

# Bandgap Formation in Topological Metamaterials with Spatially Modulated Resonators

Joshua LeGrande,<sup>1</sup> Arun Malla,<sup>1</sup> Mohammad Bukhari,<sup>2</sup> and Oumar Barry<sup>1, a)</sup>

<sup>1)</sup>*VibRo Lab, Department of Mechanical Engineering, Virginia Polytechnic University, Blacksburg, VA, 24060*

<sup>2)</sup>*Department of Mechanical Engineering, Wayne State University, Detroit, MI, 48202*

(Dated: 8 May 2024)

Within the field of elastic metamaterials, topological metamaterials have recently received much attention due to their ability to host topologically robust edge states. Introducing local resonators to these metamaterials also opens the door for many applications such as energy harvesting and reconfigurable metamaterials. However, the interactions between phenomena from local resonance and modulation patterning are currently unknown. This work fills that gap by studying multiple cases of spatially modulated metamaterials with local resonators to reveal the mechanisms behind bandgap formation. Their dispersion relations are determined analytically for infinite chains and validated numerically using eigenvalue analysis. The inverse method is used to determine the imaginary wavenumber components from which each bandgap is characterized by its formation mechanism. The topological nature of the bandgaps is also explored through calculating the Chern number and integrated density of states. The band structures are obtained for various sources of modulation as well as multiple resonator parameters to illustrate how both local resonance and modulation patterning interact together to influence the band structure. Other unique features of these metamaterials are further demonstrated through the mode shapes obtained using the eigenvectors. The results reveal a complex band structure that is highly tunable, and the observations given here can be used to guide designers in choosing resonator parameters and patterning to fit a variety of applications.

## I. INTRODUCTION

Man-made structures with specially designed configurations and constituents, known as metamaterials, have received great attention recently due to their ability to possess properties not found in natural homogeneous materials<sup>1,2</sup>. While originally developed for electromagnetic and optical wave propagation<sup>3</sup>, the technology has since expanded to include acoustic<sup>4</sup> and mechanical wave propagation<sup>5</sup>. The unique properties of these metamaterials are valuable for a large variety of applications including vibration and noise control<sup>6</sup>, energy harvesting<sup>7</sup>, mechanical computing<sup>8</sup>, structural health monitoring<sup>9</sup>, and cloaking<sup>10</sup>.

Mechanical metamaterials are commonly arranged in carefully designed configurations such as periodic<sup>1</sup>, quasiperiodic<sup>11</sup>, or random<sup>12</sup> patterns. These patterns offer exceptional dynamical properties. For instance, periodic patterning enables the formation of a bandgap in the frequency response due to Bragg Scattering. Within this bandgap, waves are forbidden from propagating and instead get reflected by the material<sup>13–18</sup>. The frequency of these bandgaps corresponds to wavelengths near the lattice constant. This allows for low frequency vibration attenuation and control. However, limitations of the lattice dimensions limit the application of this bandgap to larger structures and low frequency vibrations<sup>1</sup>.

To overcome this requirement, local resonators can be embedded inside the structure to form locally resonant metamaterials<sup>19</sup>. The local resonators open up a bandgap at wavelengths much larger than the lattice constant. These

bandgaps are formed as a result of Bragg scattering and mode hybridization, and they depend strongly on the resonator parameters<sup>20</sup>. Note that in the presence of local resonators, Bragg scattering is not essential because very low frequency resonators can still be excited by long wavelength waves. Therefore, bandgaps can still be formed in the absence of periodicity and in metamaterials with random configurations<sup>12</sup>.

While locally resonant metamaterials hold many improvements in vibration attenuation over periodic structures, they are only effective near their design frequency. For this reason, much work has been done recently to widen the range of operating frequencies. Some studies have included multiple resonators with different resonator frequencies to produce multiple bandgaps at different frequency ranges<sup>6,21,22</sup>. Others have used different kinds of resonators to broaden the bandgap such as bistable resonators<sup>23</sup> and alternately coupled resonators<sup>24</sup>. Introducing patterns into the spacing or parameters of the resonators has also been shown to be an effective method for broadening or opening new bandgaps<sup>25,26</sup>. In order to produce more adaptable locally resonant metamaterials, electromechanical elements have also been introduced through piezoelectric resonators. Studies have shown that by shunting these resonators to circuits, the locally resonant bandgaps can be actively tailored by the circuit parameters without need for changing the geometric or material parameters of the resonators<sup>27–30</sup>. In addition to this, nonlinear phenomena have demonstrated great value in enhancing bandgap control and size. With nonlinear resonators, nonlinear frequency shifts can occur in all wavelengths allowing for more broadband use<sup>31</sup>. Nonlinear Coriolis and centrifugal forces have also been utilized to design resonators that can slide to passively tune themselves to the input wave frequency<sup>32,33</sup>.

Metamaterials with spatial modulation patterns, such as quasiperiodic arrangements, have been shown to greatly en-

<sup>a)</sup>Electronic mail: obarry@vt.edu

hance vibration control and energy harvesting through the appearance of additional bandgaps and topologically protected edge modes. While periodic and locally resonant metamaterials produce topologically trivial bandgaps, quasiperiodic metamaterials are known to host multiple robust topologically protected modes that do not propagate inside the bulk and are localized within lower dimensions<sup>34</sup>. These topological modes are manifested passively through the breaking of spatial inversion symmetry while holding time-reversal symmetry<sup>35–37</sup>. One method to achieve this is through the quasiperiodic modulation of parameters within the structure following patterns such as the Aubry-André model<sup>38</sup> as seen in<sup>11,39–45</sup>. When plotted, the band structures for these metamaterials are analogous to the Hofstadter butterfly<sup>46</sup> with multiple additional non-trivial topological bandgaps appearing within the bulk propagation zones of periodic structures. Each of these bandgaps is spanned by a topological edge mode which host localized vibrations in finite chains<sup>41</sup>. By introducing a phase variable, these edge modes can be pumped from one edge to the other<sup>47–49</sup>.

Although locally resonant metamaterials have shown superior dynamical properties over other metamaterials, little work has been done to explore their arrangement with spatial patterning, thus revealing their topological features. A locally resonant quasiperiodic metamaterial is first proposed in<sup>43</sup> with quasiperiodic patterning present in the location of identical resonators along a continuous beam. Due to the combination of effects, the bulk spectrum is analogous to the Hofstadter butterfly with multiple topological bandgaps along with a single topologically trivial bandgap determined by the parameters of the resonators. A discrete quasiperiodic chain is studied in<sup>50</sup> with quasiperiodic modulation of the main chain springs and identical electromechanical resonators. It is demonstrated that weak electromechanical coupling does not impact the band structure. Quasiperiodic modulation of resonator parameters is seen in<sup>51</sup> which experimentally plots the Hofstadter butterfly and demonstrates localized vibrations. This reveals the possibility to introduce topological effects purely in the resonators allowing for advanced wave control and topological phenomena to be present in materials that must remain homogeneous for structural, load bearing, or other reasons. By introducing both spatial and temporal modulation to local resonator parameters, multiple works<sup>52,53</sup> have even broken reciprocity and demonstrated one-way wave propagation.

In spite of these works, the interactions between local resonance and spatial patterning remain ambiguous. The mechanisms behind bandgap formation in metamaterials with modulated resonator parameters are unknown, and hence, design and tuning of these metamaterials remains elusive. In this paper, we examine a system of topological metamaterials with spatially modulated local resonators to investigate the interactions between local resonance and topological effects for bandgap formation. The system consists of a spring-mass chain with each mass coupled to a local resonator. Multiple cases are studied in which the modulation patterning is present in the main chain stiffness, resonator stiffness, resonator mass, or a combination of those sources. The dispersion relation of

the infinite chain is determined from the analytical solution of a single unit cell. Results are then validated through the numerical solution of a finite chain using eigenvalue analysis for band structures and eigenvectors for mode shapes. The system is compared to previous metamaterials with modulation in the main chain to observe the effect of the modulation location. The bandgaps are characterized by both their formation mechanism and topological nature through analysis of the inverse dispersion relations and Chern number. Furthermore, resonator parameters are varied to determine their influence on the topological bandgaps.

## II. MATHEMATICAL MODELING OF THE SYSTEM

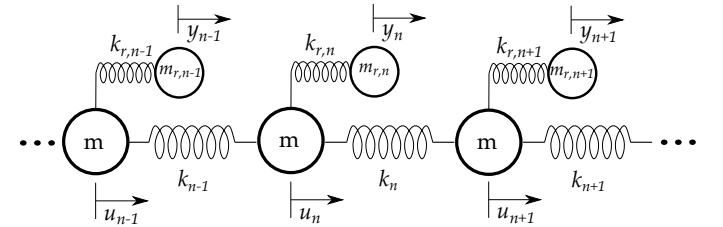


FIG. 1. Schematic of metamaterial consisting of a spring mass chain with local resonators and with spatial modulation in the main spring stiffness,  $k_n$ , resonator stiffness,  $k_{r,n}$ , and resonator mass,  $m_{r,n}$ .

This work considers 1-dimensional locally resonant metamaterials with spatial modulation in a variety of parameters as shown in Fig. 1. The metamaterial is represented by a spring-mass chain of identical masses,  $m$ , joined by springs with stiffness,  $k$ . Each mass is also coupled to a local resonator with mass,  $m_r$  and stiffness,  $k_r$ . Spatial modulation is included in either the main spring stiffness, resonator mass, resonator stiffness, or a combination of these locations. The modulation follows the Aubry-André Model<sup>38</sup> such that the  $n^{\text{th}}$  modulated parameter,  $Z_n$  is defined as

$$Z_n = Z_0[1 + \lambda \cos(2\pi n\theta + \phi)] \quad (1)$$

with average value,  $Z_0$ , and modulation amplitude,  $\lambda$ . This pattern is defined by its quasiperiodic parameter,  $\theta$ , and phase shift,  $\phi$ . Rational and irrational values of  $\theta$  produce periodic and quasiperiodic patterns, respectively. The governing equations of motion for the  $n^{\text{th}}$  mass and resonator are

$$m\ddot{u}_n + k_{n-1}(u_n - u_{n-1}) + k_n(u_n - u_{n+1}) + k_{r,n}(u_n - y_n) = 0 \quad (2)$$

$$m_{r,n}\ddot{y}_n + k_{r,n}(y_n - u_n) = 0 \quad (3)$$

where  $u_n$  and  $y_n$  are the displacements of the  $n^{\text{th}}$  mass and resonator, respectively. We impose a Bloch periodic solution of

$$u_n = \bar{U}_n e^{i(\mu n - \omega t)} \quad y_n = \bar{Y}_n e^{i(\mu n - \omega t)} \quad (4)$$

where  $\bar{U}_n$  and  $\bar{Y}_n$  are the mass displacement and resonator displacement amplitudes, respectively, with frequency,  $\omega$ , time,  $t$ , and non-dimensional wavenumber  $\mu$ . This will yield the new governing equations

$$\begin{aligned} &(-m\omega^2 + k_{n-1} + k_n + k_{r,n})\bar{U}_n - k_{n-1}\bar{U}_{n-1}e^{-i\mu} \\ &-k_n\bar{U}_{n+1}e^{i\mu} - k_{r,n}\bar{Y}_n = 0 \end{aligned} \quad (5)$$

$$(-m_{r,n}\omega^2 + k_{r,n})\bar{Y}_n - k_{r,n}\bar{U}_n = 0 \quad (6)$$

To obtain an analytical expression for the dispersion relations of an infinite chain, a single unit cell will be studied. The equations of motion for the  $j^{\text{th}}$  unit cell can be expressed

$$\mathbf{K} = \begin{bmatrix} k_1 + k_3 + k_{r,1} & -k_1 e^{i\mu} & -k_3 e^{-i\mu} & -k_{r,1} & 0 & 0 \\ -k_1 e^{-i\mu} & k_1 + k_2 + k_{r,2} & -k_2 e^{i\mu} & 0 & -k_{r,2} & 0 \\ -k_3 e^{i\mu} & -k_2 e^{-i\mu} & k_2 + k_3 + k_{r,3} & 0 & 0 & -k_{r,3} \\ -k_{r,1} & 0 & 0 & k_{r,1} & 0 & 0 \\ 0 & -k_{r,2} & 0 & 0 & k_{r,2} & 0 \\ 0 & 0 & -k_{r,3} & 0 & 0 & k_{r,3} \end{bmatrix} \quad (8)$$

To validate the analytical dispersion relations, numerical simulation is used to obtain the natural frequencies of finite chains from the eigenvalues over the full range of the phase variable,  $\phi$ . Furthermore, the mode shapes are also determined numerically from the system eigenvectors.

### III. RESULTS

To best understand the dynamic interactions between local resonance and spatial modulation, we will consider here four cases determined by where the modulation is present in the chain. Case one will have modulation in the stiffness of the main springs with identical (i.e. periodic) resonators. The remaining three will have modulation present in the local resonator parameters. Case two will modulate the resonator stiffness, and case three will modulate the resonator mass. Case four will modulate both the resonator stiffness and mass in such a way that the natural frequency of the local resonators remains constant. Both infinite and finite chains will be studied with 60 cells in the finite chains. A quasiperiodic parameter of  $\theta = 1/3$  will be used, producing a unit cell of three masses and resonators. Except where stated otherwise, the systems will have the following parameters:  $m = 1$  kg,  $m_{r,0} = 0.2$  kg,  $k_0 = 1$  N/m,  $k_{r,0} = 0.3$  N/m, and  $\lambda = 0.6$ . The phase angle,  $\phi$ , will be varied through the full range from 0 to  $2\pi$ . For the modulated parameters, the subscript 0 denotes the average value.

In this section, we will explore how both the band structure and mode shapes of each case are determined by the interactions between spatial modulation and local resonance. We start by comparing the band structures for each case to ob-

in matrix form as

$$(-\mathbf{M}\omega^2 + \mathbf{K})\mathbf{u}_j = 0 \quad (7)$$

where  $\mathbf{M}$  is the mass matrix,  $\mathbf{K}$  is the stiffness matrix, and  $\mathbf{u}_j$  is the vector of mass and resonator displacements,  $\mathbf{u}_j = [\bar{\mathbf{U}}; \bar{\mathbf{Y}}]$ . To obtain nontrivial solutions to Eq. 7, the coefficient matrix must be singular. By setting the determinant equal to zero, the characteristic equation can be obtained. From this characteristic equation, the dispersion relation is determined. For a chain with  $N$  masses in its unit cell, the mass and stiffness matrices are  $2N \times 2N$ , and the characteristic equation has  $2N$  roots yielding  $2N$  bands in the dispersion relation. For this study, we will consider a chain with quasiperiodic parameter  $\theta = 1/3$  ( $N = 3$ ) with stiffness matrix

serve how the location of modulation impacts the band structure. From there, further parametric analysis demonstrates how proper tuning of resonator parameters can be leveraged alongside modulation to shape the band structure. Finally, the mode shapes are displayed to examine how unique properties of the band structure impact the localized vibration modes of the systems.

#### A. Effect of Spatial Modulation Location

Calculating the roots to the characteristic equation obtained from equation 7 yields the 3D dispersion surfaces shown in Fig. 2. Here, the frequency is given as the nondimensional frequency,  $\Omega = \omega/\omega_0$  where  $\omega_0 = \sqrt{k_0/m}$ , and it is a function of the dimensionless wavenumber,  $\mu$ , and phase variable,  $\phi$ . The six roots of the characteristic equation produce a dispersion relation with six passband surfaces separated by five bandgaps for each case. In general, there is little difference between cases as the wavenumber is varied. The one exception to this is that for cases with modulation in one resonator parameter (cases two and three), there are occasionally passbands showing opposite trends with changes in wavenumber. For example, in case two, in Fig. 2(b), the fourth (light blue) passband decreases in frequency as the wavenumber approaches  $\pi$  whereas the fourth passband increases for each other case. Similarly, the second (green) passband in case three, shown in Fig. 2(c), increases as the wavenumber approaches  $\pi$  whereas the second passband decreases for each other case.

With variation in the phase angle,  $\phi$ , however, there are more significant changes from case to case. Especially for cases two and three, the middle passbands show significant

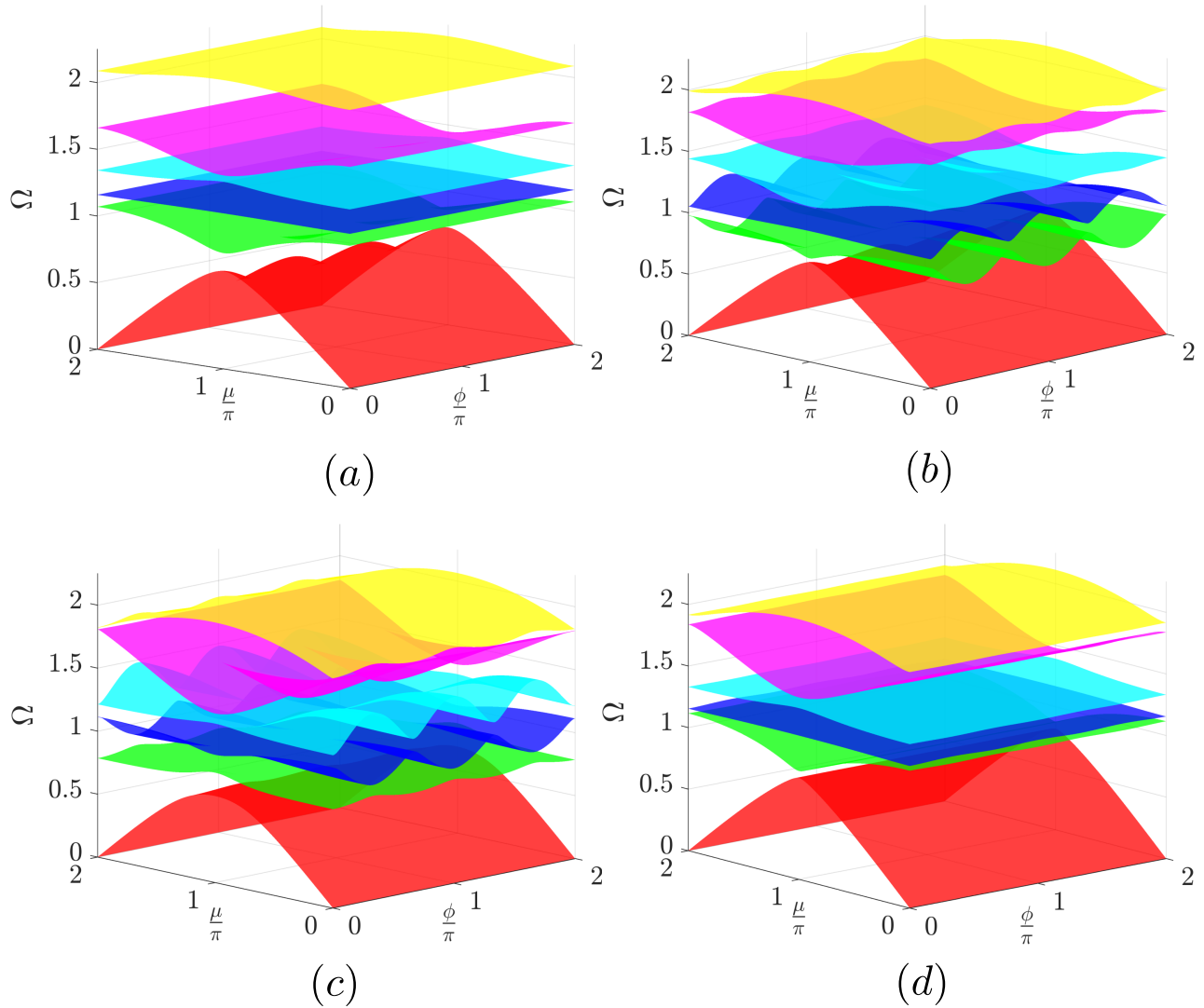


FIG. 2. Infinite dispersion relations detailing dimensionless wavenumber,  $\Omega$ , as a function of dimensionless wavenumber,  $\mu$ , and phase variable,  $\phi$ , for (a) case one, with modulation in main cell stiffness,  $k$ , (b) case two, with modulation in the resonator stiffness,  $k_r$ , (c) case three, with modulation in the resonator mass,  $m_r$ , and (d) case four, with modulation in the resonator stiffness,  $k_r$ , and mass,  $m_r$ .

periodic oscillations while the first and fourth cases do not. Furthermore, variation in phase angle can reveal meaningful trends in topological phenomena in finite chains such as topological pumping, demonstrated in Section 3C. For these reasons, the following analysis will primarily focus on variation in phase angle,  $\phi$  for both the finite and infinite chains.

Although changing the location of parameter modulation from the main cells (case one) to the resonator parameters (cases 2-4) does not change the number of bandgaps in the frequency spectrum, the behavior of the bandgaps can still be significantly altered. By introducing multiple resonator frequencies in cases two and three, there is the possibility for coupling bandgap formation mechanisms (i.e. local resonance and Bragg scattering) within pre-existing bandgaps. Such behavior has been previously reported in work by Gao and Wang<sup>22</sup> in which a hybrid metamaterial with different multi-resonator unit cells displayed bandgaps with coupled behav-

ior of both local resonance and Bragg scattering. To characterize the mechanisms behind bandgap formation, the inverse method is used on the characteristic equation to obtain the real and imaginary components of the wavenumber at a given frequency. From the imaginary component of the wavenumbers, the bandgap mechanism can be determined based on criteria developed by Liu and Hussein<sup>20</sup>.

The real and imaginary wavenumber components are given in Fig. 3 for each case. In this representation, bandgaps produced by Bragg scattering yield attenuation zones with imaginary wavenumbers that are symmetric and roughly semicircular. On the other hand, locally resonant bandgaps produce asymmetric attenuation zones with a much stronger peak centered on the natural frequency of the resonator. The natural frequency for each resonator, defined as  $\omega_{r,n} = \sqrt{k_{r,n}/m_{r,n}}$ , is shown here as a dashed blue line. In case one, shown in Fig. 3(a), there is only one resonator frequency and only one

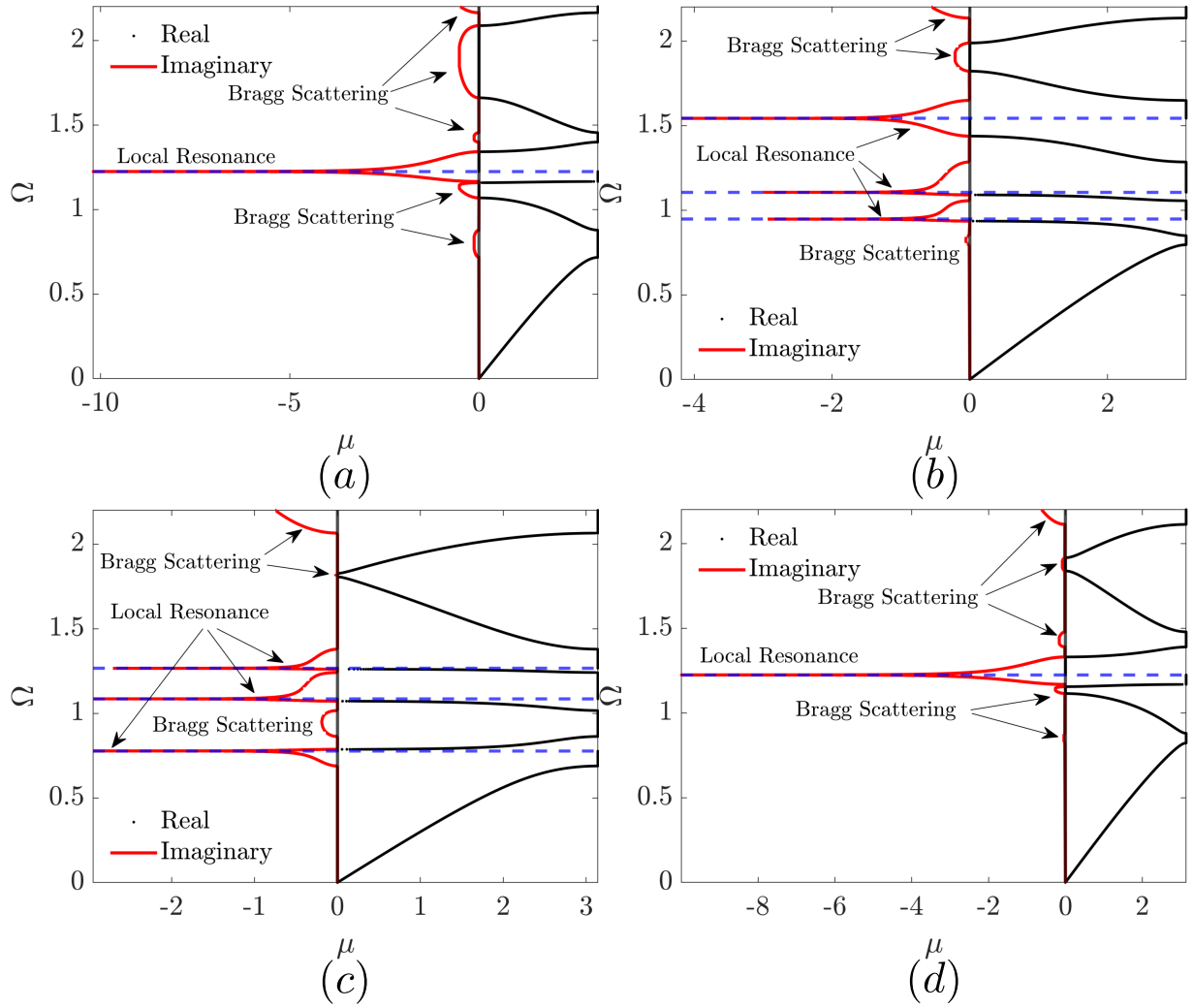


FIG. 3. Real and imaginary wavenumber components as a function of frequency for cases 1-4 (a)-(d), respectively, with phase  $\phi - \phi_0 = 0.6\pi$ . Nonzero imaginary components, shown in red, indicate the existence of a bandgap with the formation mechanism labeled for each bandgap. The resonator frequencies are shown by the dashed blue lines.

locally resonant bandgap corresponding to it. The remaining bandgaps are all due to Bragg scattering. This same behavior is seen in case four (Fig. 3(d)) since this case also only has one resonator natural frequency. For cases two and three however, there are three locally resonant bandgaps with peaks matching the three natural frequencies of the resonators. Compared to the Bragg scattering bandgaps, the locally resonant bandgaps show much stronger attenuation. Due to this, introducing modulation to the resonator parameters can produce significant improvements to the vibration attenuation performance of these metamaterials.

As mentioned previously, changing the modulated parameter can alter the dispersion relation as it varies with the phase,  $\phi$ . To analyze this further, the finite and infinite band structures are plotted for all four cases in Fig. 4. The bulk dispersion bands for the infinite chain are shown in grey with the natural frequencies of the finite chain overlaid as black lines. The additional topological edge modes that span the bandgaps are highlighted in red, and the natural frequencies

of the resonators are displayed as dashed blue lines. The first case studies a chain with identical resonators and spatial modulation in its main cell stiffnesses. While the primary focus of this paper is on cases with modulated resonators, a brief discussion of case one is given to be used as a baseline standard of comparison for the remaining three cases. A more thorough analysis of this case can be found in<sup>50</sup>. For case one, we see that the band structure in Fig. 4(a) consists of six bulk bands split by five bandgaps. Four of the bandgaps each contain a single topologically non-trivial edge mode, while the middle bandgap is topologically trivial, with no edge mode present. This trivial bandgap is centered on the single natural frequency of the resonators, and it evenly splits the dispersion bands with three passbands above it and three below.

After investigating the topological features of modulation in the stiffness of the main springs, we examine modulation in the local resonators. Indeed, unlike other metamaterials, locally resonant metamaterials allow us to achieve patterning through modulating the local resonator parameters. This will

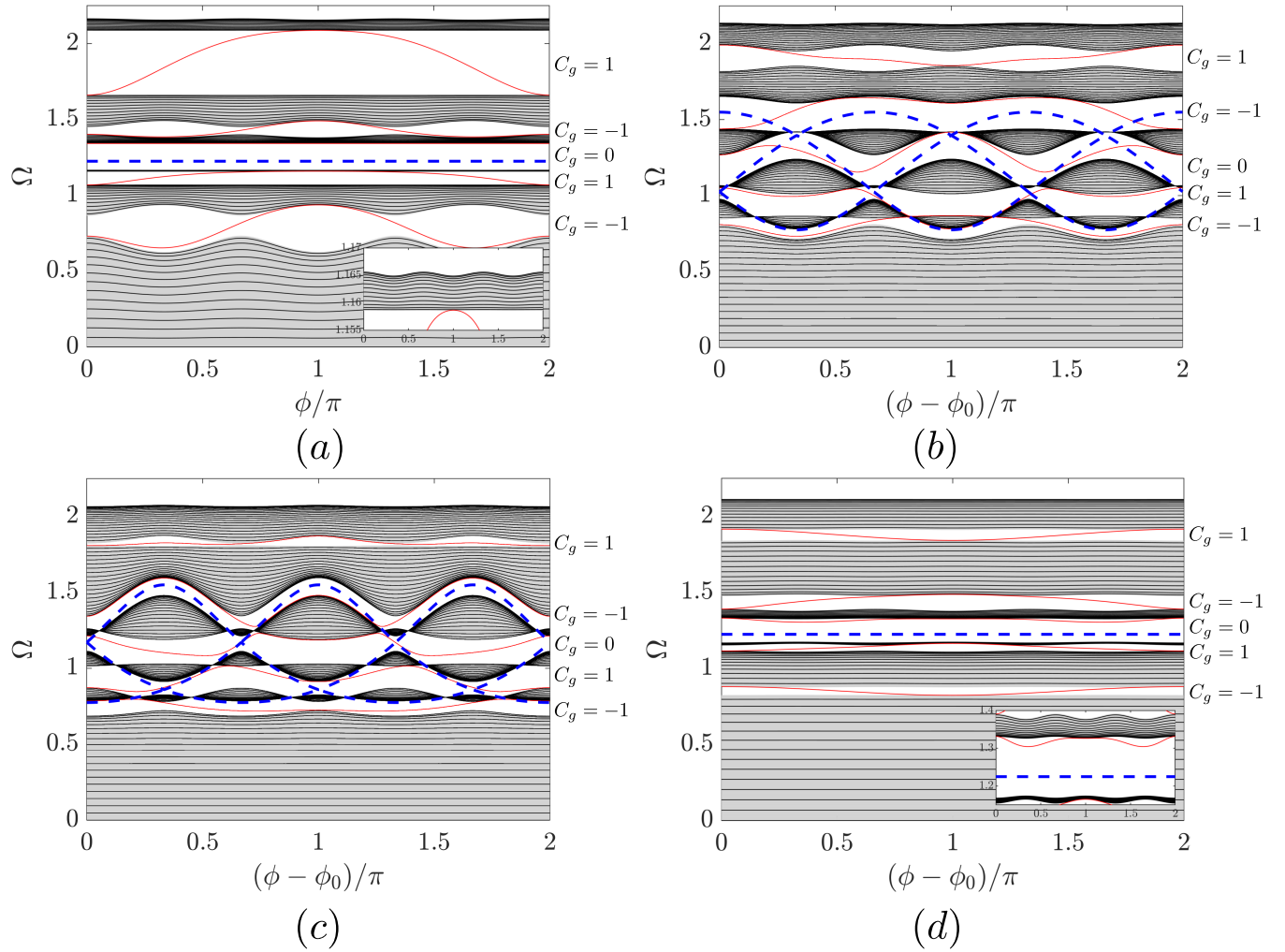


FIG. 4. Band structure for an infinite (grey background) chain and finite (black lines) chain of 60 cells with modulation present in (a) the main spring stiffness (case one), with inset figure zooming in on the third passband, (b) the resonator stiffness (case two), (c) the resonator mass (case three), and (d) both the resonator stiffness and mass (case four), with inset figure zooming in on the third and fourth passbands. Edge modes spanning the bandgaps are shown as red lines, and the resonator natural frequencies are shown as dashed blue lines. The Chern number for each bandgap is also labeled. Cases 2-4 are shifted by phase shift  $\phi_0$ .

be investigated in the remaining three cases. While there are some similarities, there are also many significant differences to discuss. We can see that for every case, there are still six passbands and five bandgaps as well as multiple edge modes spanning the topological bandgaps. However, one major difference is a shift in the initial placement of the edge modes at phase  $\phi = 0$  for cases with modulated resonator parameters (cases 2-4). As seen in Fig. 4, varying the phase angle causes the topological bandgaps to grow and shrink while also moving the edge states within the bandgaps. By moving the edge state nearer or further from the bulk bands, one can improve the degree of localization in the chain as well as change the localization edge. This has been used as a primary method to achieve topological pumping<sup>11,47-49,54</sup> and nonreciprocal wave propagation<sup>53,55-57</sup>. As such, it is incredibly important to know how the edge states migrate with the phase value. For previously studied cases with modulation only in the main chain, the movement of the edge states has been symmetric

about the phase  $\phi = \pi$ , touching the bulk bands at  $\phi = 0$  or  $2\pi$  and at  $\phi = \pi$ . This is demonstrated in case one in Fig. 4(a) with modulated  $k$ . However, when modulation is introduced to the resonators instead, as in cases 2-4 (Fig. 4(b)-(d)), the edge states undergo a phase shift and are no longer symmetric about  $\phi = \pi$ . The results presented in Fig. 4(b)-(d) are shifted by a phase,  $\phi_0$ , to maintain symmetry. The original band structures without the phase shift are given for cases two and three in Fig. 5. Without the phase shift, the points of symmetry, which correspond to the points of contact with the bulk bands, are found instead to be at  $\phi = 2\pi/3$  and  $\phi = 5\pi/3$ . While they are not included here for brevity, similar results were also obtained for other values of the quasiperiodic parameter. From these results, it was determined that the phase shift is directly related to the quasiperiodic parameter and can be quantified as

$$\phi_0 = \pm(1 - \theta)\pi \quad (9)$$

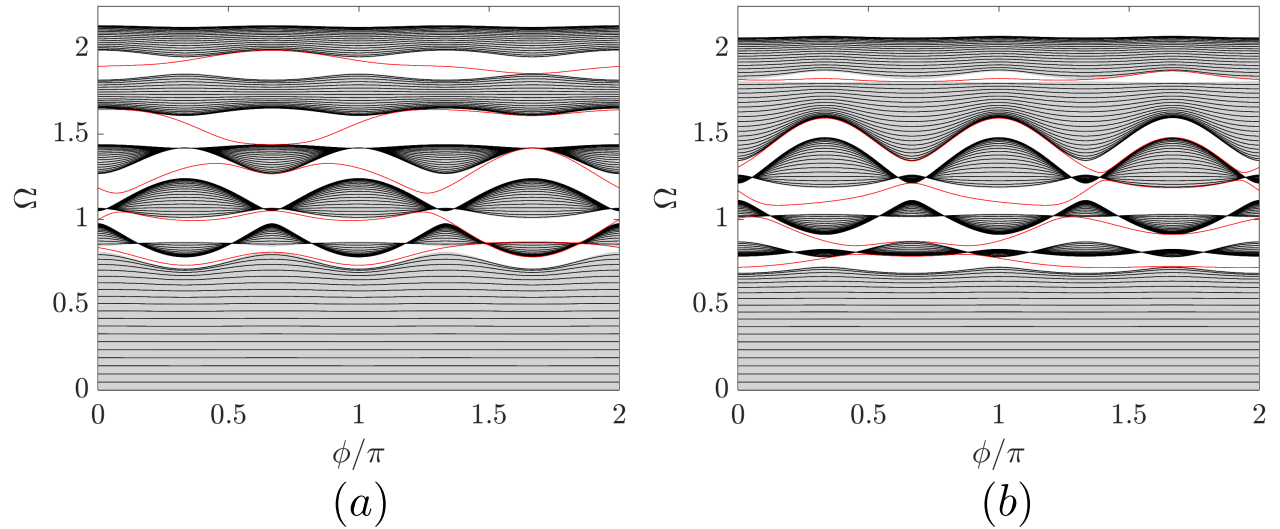


FIG. 5. Band structure for an infinite (grey background) chain and finite (black lines) chain of 60 cells with modulation present in the resonator (a) stiffness (case two) and (b) mass (case three) without phase shift,  $\phi_0$ , leading to asymmetric edge modes, highlighted as red lines.

Since there are two points of symmetry in the edge state, the phase could be shifted in either direction to a point of symmetry. For the specific case of  $\theta = 1/2$ , symmetry is already achieved, and no phase shift is necessary. In all figures, the positive phase shift will be included whenever modulation is present in the resonator parameters.

With modulation in just one of the local resonator parameters, such as in cases two (Fig. 4(b)) or three (Fig. 4(c)), there is not just one resonator frequency, but multiple. In the systems studied here with  $\theta = 1/3$ , there are three. These three resonator frequencies have a significant impact on the band structure of the system, and it is crucial to understand how their interactions lead to bandgap formation. Because there are multiple resonator frequencies, we will discuss not only the individual frequency values, but also the resonator frequency range. This range is defined in terms of both its size and location, where the size is the difference between the highest and lowest resonator frequencies, and the location is at the average resonator frequency,  $\omega_{r,0} = \sqrt{k_{r,0}/m_{r,0}}$ . This frequency range highlights the effects of varying the source of modulation, and it can be visualized in Fig. 4(b)-(c) as the area between the upper and lower dashed blue lines. Even when the resonator parameters ( $k_{r,0}$  and  $m_{r,0}$ ) are kept constant, the resonator frequency range may differ between cases two and three. In this section, we wish to isolate the effects of the source of modulation, while in the next section, we will explore how to manipulate the resonator frequency range. In order to accomplish this and provide a more direct comparison, different resonator parameters are used between cases two and three to produce the same resonator frequency range in Fig. 4(b)-(c). For case two, shown in Fig. 4(b) with modulated  $k_r$ , we use the standard parameters  $k_{r,0} = 0.3$  N/m and  $m_{r,0} = 0.2$  kg. For case three, shown in Fig. 4(c) with modulated  $m_r$ , we change the average stiffness to  $k_{r,0} = 0.192$  N/m and keep the mass the same. This produces a nondimensional resonator frequency range of 0.77-1.55 for both cases.

When considering how the band structure changes with the phase angle,  $\phi$ , the multiple resonator frequencies of cases two and three result in a much higher sensitivity to the phase angle. The effects of this are largely present within the resonator frequency range itself. In general, the passbands and bandgaps undergo larger variation with the phase angle as shown in Fig. 4(b)-(c). This includes the middle (trivial) bandgap which shows no significant variation for cases one and four as seen in Fig. 4(a) and (d). In addition, Fig. 4(b)-(c) indicate that this middle bandgap still appears centered near the average natural frequency of the resonators,  $\omega_{r,0}$ , but its width is no longer constant and varies periodically with the phase.

Perhaps the most significant impact of having multiple resonator frequencies in cases two and three is that there are multiple points at which the passbands shrink to zero width and disappear, causing the two adjacent bandgaps to merge. These occur at points where the passband is crossed by one of the frequencies of the resonators. As the resonator frequency approaches the passband, the passband shrinks until it eventually produces a bandgap where the resonator frequency crosses the passband. These points are also closely tied to where two resonator frequency values converge. For example, in Fig. 4(c), the fourth passband shrinks to zero width as resonator frequencies cross it at  $\phi = 0.61\pi$  and  $0.72\pi$ . These points lie on either side of the crossing of two resonator frequencies at  $\phi = 0.67\pi$ . This shrinking of passbands indicates, for the first time, the ability to change the number of bandgaps and passbands in a spatially modulated system without changing the modulation pattern. A locally resonant system with  $\theta = 1/3$  has always been shown to have six passbands with five bandgaps. But with modulation in the resonators and an appropriate choice of phase variable, it is possible to instead have five passbands with four bandgaps. This is seen again in Fig. 4(c). At the point  $\phi = 0.61\pi$ , when the fourth passband closes, the band structure has only five passbands and

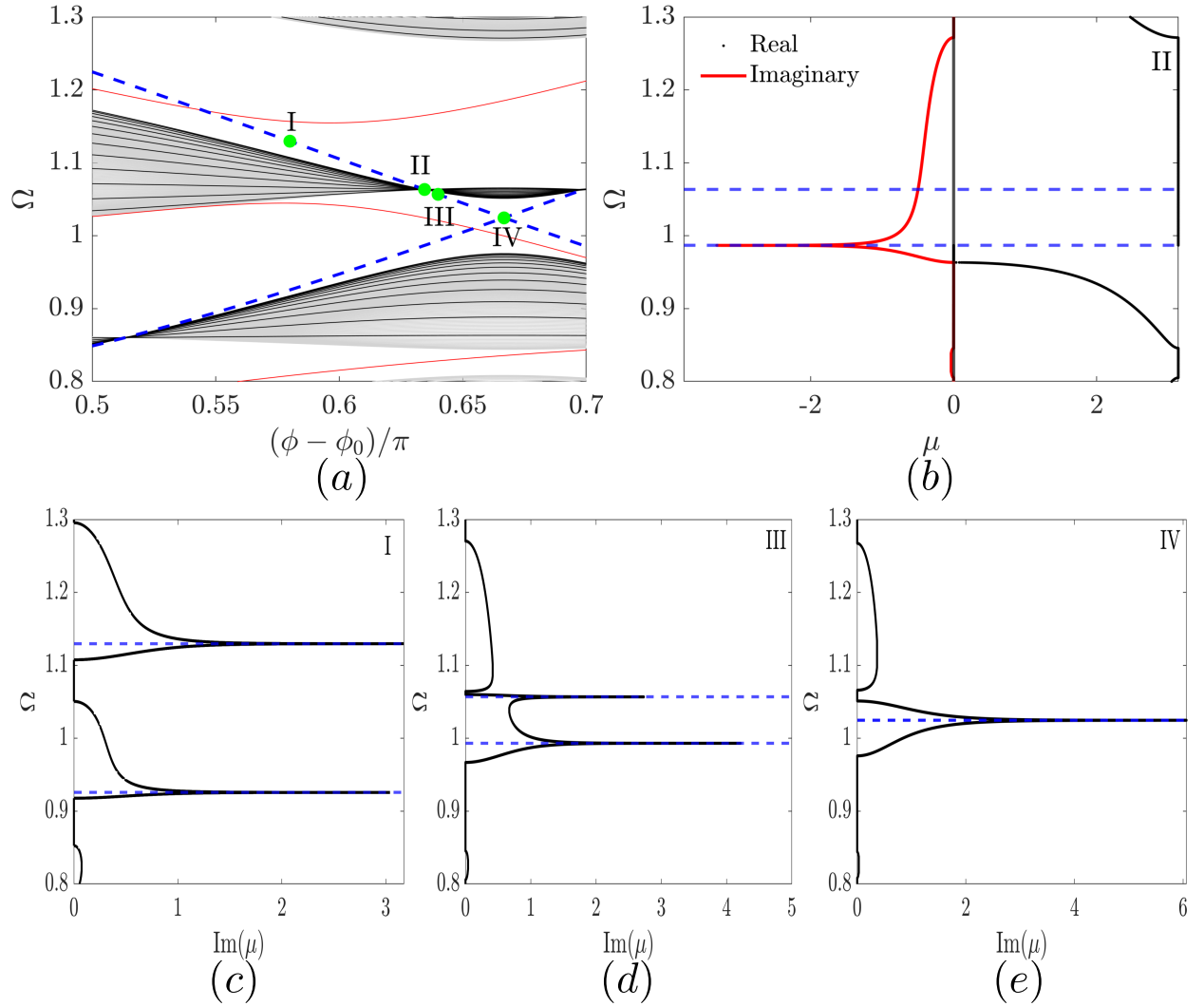


FIG. 6. (a) Zoomed-in band structure of case two from Fig. 4(b), displaying the intersection of two resonator frequencies within the second bandgap and the crossing of the third passband by a resonator frequency. Four points of interest are highlighted at  $\phi - \phi_0 = 0.58\pi$ ,  $0.6345\pi$ ,  $0.64\pi$ , and  $0.66\pi$ . (b) The real and imaginary wavenumber components are given as a function of frequency at  $\phi - \phi_0 = 0.6345\pi$  when the resonator frequency crosses the third passband. (c)-(e) The imaginary component of the wavenumber is plotted at  $\phi - \phi_0 = 0.58\pi$ ,  $0.64\pi$ , and  $0.66\pi$ , respectively, for each point of interest, displaying how the bandgap mechanisms transition with the phase angle,  $\phi$ . The resonator frequencies are shown by the dashed blue lines.

four bandgaps.

At these critical transition points, the resonator natural frequency crosses from one bandgap into another, often joining a second resonator frequency within the same bandgap. As the resonator frequency transitions from one bandgap to the next, it also changes the nature of the bandgaps it is leaving and entering. This can be observed through the imaginary components of the wavenumber as the transition is made. One example of this is found in the second case, when the middle resonator frequency crosses from the third bandgap into the second bandgap near  $\phi - \phi_0 = 0.63\pi$ . A close-up view of this frequency crossing is shown in Fig. 6(a) alongside the wavenumber components at the point of crossing in Fig. 6(b) and the imaginary component of the wavenumbers at three other critical points in Fig. 6(c)-(e). At point (I), both resonator frequen-

cies are in separate bandgaps, and both bandgaps are formed by local resonance, as displayed in Fig. 6(c). At point (II), in Fig. 6(b), the upper resonator frequency is coincident with the third passband, causing the passband to disappear and the adjacent bandgaps to merge. Looking to the real component of the wavenumber, there exist only five passbands instead of six. Furthermore, from the imaginary component of the wavenumber, it is evident that the second resonant peak has disappeared. The single merged bandgap displays the width common among Bragg scattering bandgaps as well as one peak at the frequency of the lower resonator frequency. After the upper resonator frequency crosses the third passband, the two resonator frequencies coexist within the second bandgap. An example of this is highlighted by point (III) in Fig. 6(d). This results in the third bandgap transitioning to a Bragg scatter-

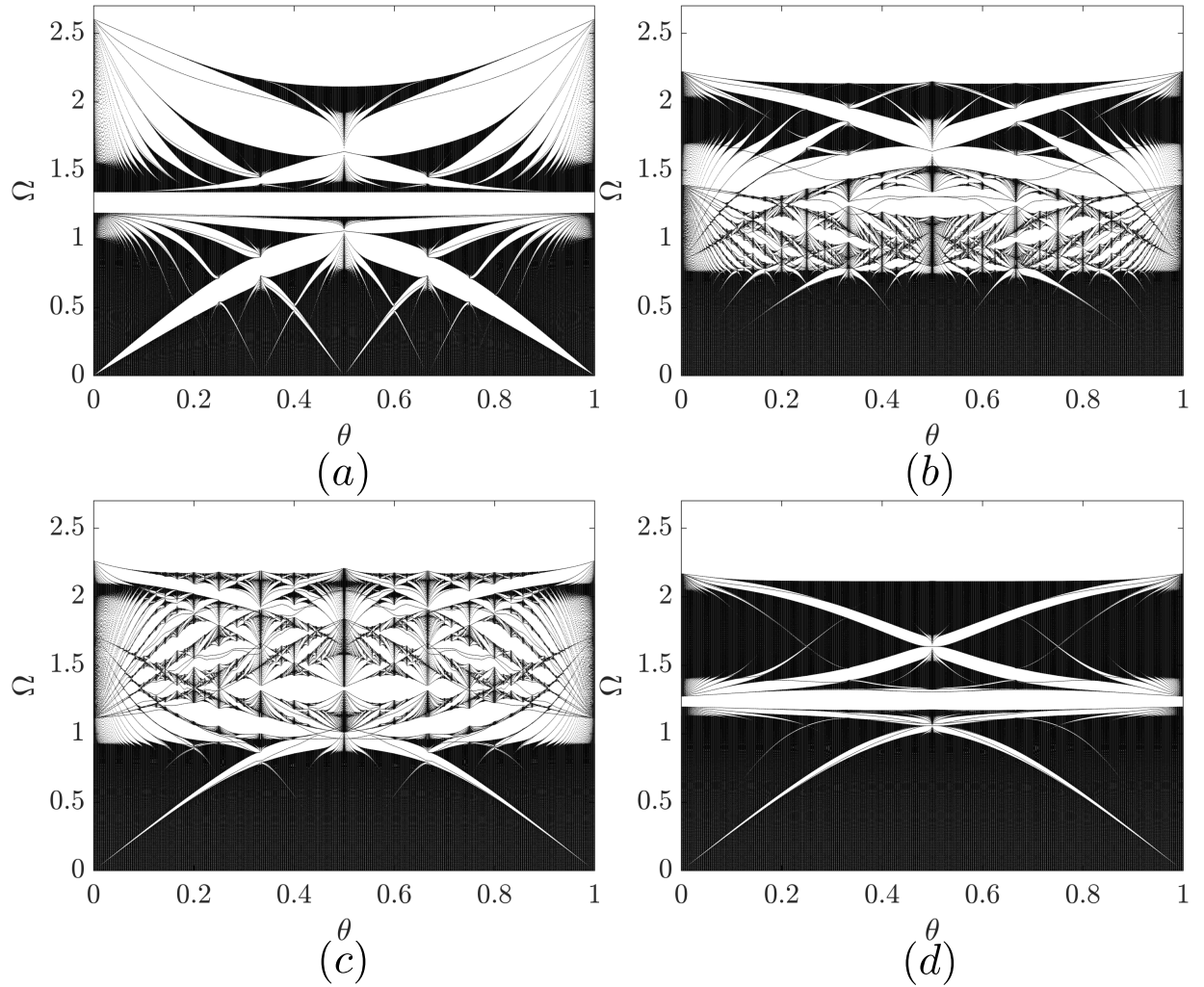


FIG. 7. Spectrum of natural frequencies for a chain of 1000 cells with  $\phi - \phi_0 = 0$  and variation over the full range of the quasiperiodic parameter,  $\theta$  for cases 1-4 (a)-(d), respectively. The standard parameters are used for  $k_{r,0}$  and  $m_{r,0}$ . The spectra resemble the Hofstadter butterfly with the ‘wings’ representing significant bandgaps.

tering bandgap while the second bandgap obtains two attenuation peaks. At point (IV), shown in Fig. 6(e), the two resonator frequencies are identical, causing the lower bandgap to again have a single peak while the upper bandgap remains as a Bragg scattering bandgap. This transition reveals further bandgap tuning capability from modulated resonators, allowing for control over the number and location of locally resonant bandgaps through a single parameter.

In a similar fashion, the increased variation in passbands and bandgaps with the phase angle also makes it possible for two passbands to overlap in their frequency range at different phase angles. This can be seen for the first bandgap in Fig. 4(b) where the upper limit of the first passband is 0.81 and the lower limit of the second passband is 0.78. While the overlap occurs at different phase angles, it prevents the formation of a complete bandgap across all phase values, and it can be very problematic in some applications such as topological pumping. Fortunately, this can be resolved by carefully selecting resonator parameters that expand the bandgap size. This

will be demonstrated in the following section.

Another significant difference between cases with modulation in the main chain and in the resonators is the presence of an additional mode within the middle (third) bandgap. In case one, the third bandgap is topologically trivial and contains no modes within it, but for cases 2-4, there is an additional mode within the third bandgap. To understand the presence of this additional mode, it is necessary to discuss the topological nature of this bandgap. The bulk-boundary correspondence principle can be used to relate the presence of edge modes within bandgaps to the Chern number<sup>58</sup>. The Chern number is a topological invariant used to define the topological nature of the bulk bands and bandgaps. For each bulk band, the Chern number can be evaluated analytically as an integer over the domain  $(\mu, \phi) \in \mathcal{D} = [0, 2\pi] \times [0, 2\pi]$  as

$$C = \frac{1}{2\pi i} \int_{\mathcal{D}} \nabla \times \mathbf{A} d\mathcal{D} \quad (10)$$

where  $\nabla = (\partial/\partial\mu)\mathbf{e}_\mu + (\partial/\partial\phi)\mathbf{e}_\phi$  and  $\mathbf{A} = \mathbf{u}^* \cdot \nabla \mathbf{u}$  with  $(\cdot)^*$  denoting the complex conjugate. The Chern number labeling

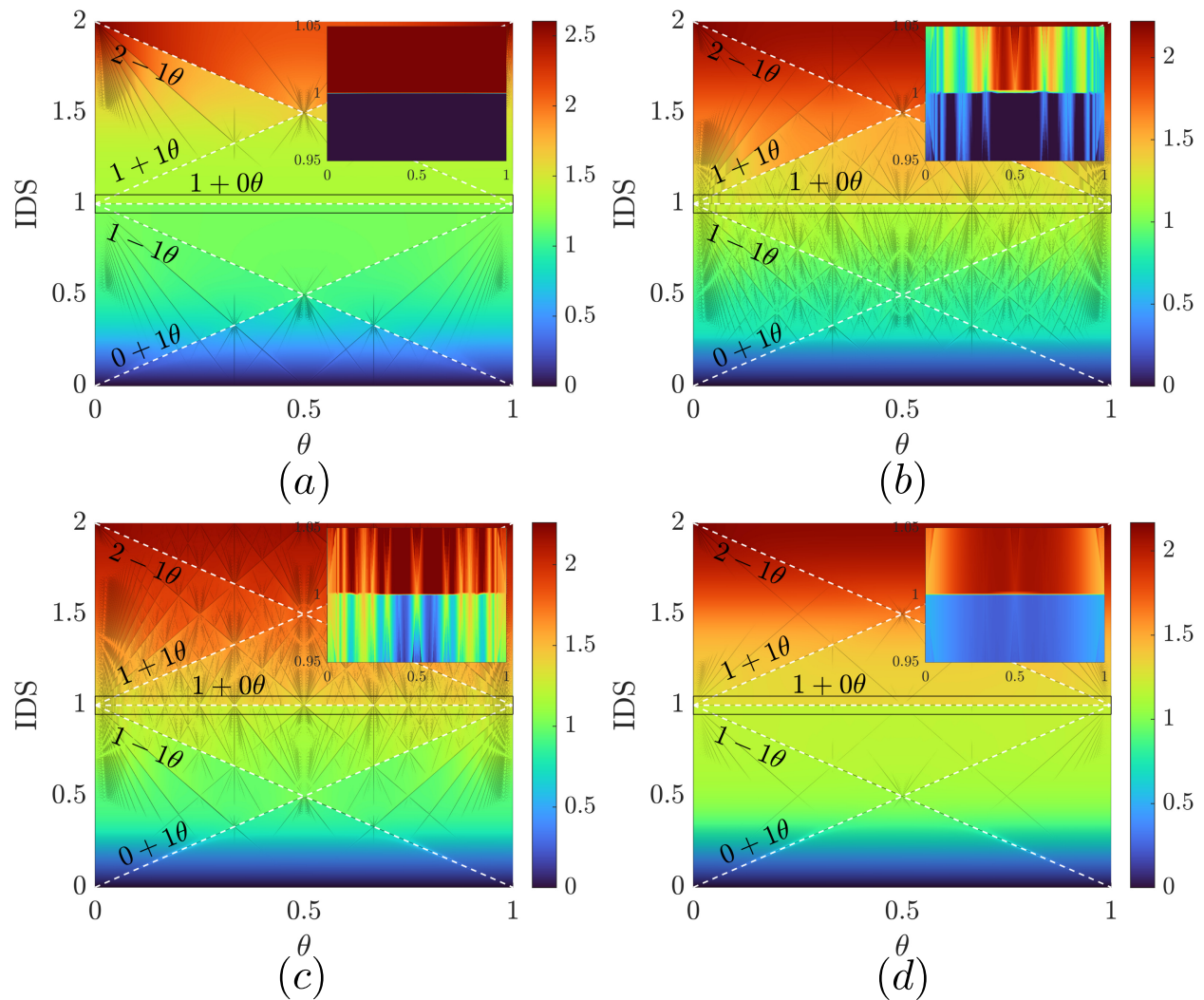


FIG. 8. Integrated Density of States for cases 1-4 (a)-(d), respectively, with  $\phi - \phi_0 = 0$ . Select bandgaps are highlighted by dashed white lines, and inset figures zoom in on the trivial bandgap highlighted by the black rectangle.

a gap,  $C_g$ , is obtained by summing the Chern numbers for each bulk band below the gap. A nonzero gap label indicates that the gap is topological and guarantees the presence of an edge mode spanning the gap from one bulk band to the other. The value of the gap label,  $|C_g|$ , is equal to the number of modes spanning the bandgap, and the sign indicates the direction of mode migration with increasing phase,  $\phi$ . While the Chern number can be evaluated using Eq. 10, direct computation is often challenging. Instead, the Chern number is evaluated numerically following the approach found in<sup>59</sup>. As shown in Fig. 4, the third bandgap has a Chern number of zero for each case while the remaining bandgaps have gap labels of  $\pm 1$ .

The Chern number for the bandgaps can also be approximated from the computed Integrated Density of States (IDS) over a spectrum of the full quasiperiodic parameter,  $\theta$ . The IDS at frequency,  $\Omega$ , is defined as

$$\text{IDS}(\Omega) = \lim_{N \rightarrow \infty} \frac{\sum_n [\omega_n \leq \Omega]}{N} \quad (11)$$

where  $\omega_n$  is the  $n^{\text{th}}$  natural frequency, and  $[\cdot]$  are the Iverson

brackets returning a value of 1 when the statement within is true and a value of 0 otherwise. In other words, the IDS at a frequency,  $\Omega$ , is a summation of the number of natural frequencies below it, normalized to the size of the chain,  $N$ . The value theoretically converges as the size approaches infinity, but it is practical here to consider a large chain of  $N = 1000$  masses. To best understand how the Chern number is calculated over a spectrum of the quasiperiodic parameter, it is worthwhile to first observe how the frequency spectrum varies with the quasiperiodic parameter. This bulk spectrum, commonly known as the Hofstadter butterfly, is shown in Fig. 7 for each case. As the name implies, the spectra emulate a butterfly shape with major and minor wings representing various bandgaps. The major ‘wings’ of the butterfly display bandgaps that change with the quasiperiodic parameter,  $\theta$ , but are always present whereas the minor ‘wings’ are not constant across all  $\theta$  values. In case one, the trivial bandgap can be clearly seen as the constant frequency bandgap splitting the bulk spectra into two separate butterflies. For cases 2-3, there

are remnants of a significant central bandgap, but their overall spectra display significant distortion from case one. Meanwhile, case four does display a constant central bandgap.

Looking now to the IDS, in Fig. 8, we can see the effects of these distortions on the topological nature of the bandgaps through the Chern number. In Fig. 8, the colormap represents the frequency, and the lines of sharp color change indicate the bandgaps. These jumps in frequency arise because all frequencies within a bandgap share the same IDS. In this representation, the bandgaps can be expressed as a line

$$\text{IDS}(\theta) = a + b\theta \quad (12)$$

with intercept,  $a$ , and slope,  $b$ . Using Streda's formula,  $\frac{\partial \text{IDS}}{\partial \theta} = C_g$ , the bandgap label is determined to be equal to the slope of the bandgap line,  $b$ . Some of these lines are highlighted in Fig. 8 as dashed white lines with their equations shown. These results agree well with the numerical calculations showing Chern numbers of -1, 0, and 1 for bandgaps with quasiperiodic parameter  $\theta = 1/3$ . Therefore, a topologically trivial bandgap can be identified as the horizontal ( $b = C_g = 0$ ) bandgap. Referring back to the butterfly spectra in Fig. 7, these horizontal trivial bandgaps line up with the constant central bandgaps splitting the spectra in half. The bandgaps with slope  $\pm 1$  represent the major 'wings' of each butterfly. Looking to the IDS plots in Fig. 8, every case contains a horizontal bandgap at  $\text{IDS} = 1$  indicating the topologically trivial nature of this bandgap.

It is made evident that moving the modulation from the main cell to the resonator parameters does not influence the topological nature of the bandgaps. However, upon closer inspection, there are minor variations in the trivial bandgaps with modulated resonator parameters. The inset figures in Fig. 8 display zoomed in views of the trivial bandgap. In case one, shown in Fig. 8(a), there is a very distinct horizontal line across all values of the quasiperiodic parameter. However, for the remaining cases in Fig. 8(b)-(d), this is not the case. While there is still a jump in color along the line  $\text{IDS} = 1$ , the line varies slightly to higher or lower IDS values, and there are multiple points along the line where the bandgap is crossed by other colors. These differences can be explained by how the trivial bandgap varies with parameter changes and by the presence of an additional mode within the bandgap. In cases two and three (Fig. 8(b)-(c)), the trivial bandgap does not remain constant for all values of the quasiperiodic parameter. While these changes can impact the trivial bandgap, they do not alter its topologically trivial nature.

With the bandgap determined to be topologically trivial, the additional mode appearing within the bandgap cannot be identified as a topological edge mode. However, other types of localized modes within the bandgaps have been previously reported in literature. One kind sharing many similar qualities is the defect mode reported in<sup>43,60</sup>. Reference<sup>43</sup> reports on a continuous beam with local resonators spaced along the beam following a quasiperiodic pattern. In that system, an additional mode appears that is dependent on the boundary conditions. In the trivial bandgap, there are no modes under pinned-pinned boundary conditions and one additional mode under clamped-free boundary conditions. Furthermore, the

additional edge mode does not span the full frequency range of the bandgap. Instead, it separates from the upper passband and returns to it without ever touching the lower passband. The same behavior is observed here in cases 2-4. The modes within the trivial bandgap do not span the bandgap. Rather, they separate from the fourth passband and return to it without touching the third passband. Despite not being a topological edge mode, these modes still display vibration localization, which will be demonstrated later.

While cases two and three are very similar to one another and display many differences from case one, case four shares some characteristics with each of the other cases. Since case four includes equal modulation in both the resonator mass and stiffness, the resonators have a single constant natural frequency as in case one rather than a resonator frequency range as in cases two and three. Because of this, the band structure for case four (Fig. 4(d)) is closest to that of case one (Fig. 4(a)). In general, the bandgaps and passbands for case four show significantly lower variation than we see in any of the other cases. Due to these nearly flat bandgaps, we do not find any overlapping passbands as can be seen in cases two and three. There are also no points at which any passbands close since the resonator frequency remains within the middle bandgap and never crosses a passband. Although case four lacks a resonator frequency range, it does still share some characteristics with cases two and three. For example, case four experiences the same phase shift in its edge modes due to the modulation in its resonators. Case four also hosts an additional edge mode within its third bandgap, shown in Fig. 4(d). Like in cases two and three, this edge mode does not span the entire bandgap but remains near to the fourth passband.

## B. Effect of modulated resonator parameters

As previously mentioned, in cases with a single modulated resonator parameter (cases two and three), the band structure and bandgap formation are strongly determined by the frequency range of the resonators. As such, it is important to know the effect of manipulating this frequency range. Because the natural frequencies of the resonators are directly influenced by the resonator stiffnesses and masses, we will now study how changes in the average values and in the modulation of these parameters can be used to control the location and size of this frequency range. It is worth noting here that while changing the resonator parameters can alter the bandgap properties, they cannot change the topological nature of the bandgaps as the Chern number remains invariant under these perturbations.

Figure 9 shows the band structure for case two with modulated resonator stiffness for varying values of average resonator stiffness,  $k_{r,0}$ , and mass  $m_{r,0}$ . Similar results are shown in Fig. 10 for case three with modulated resonator mass. To vary the mass and stiffness of the resonators, the average values are increased or decreased by a factor of three. This results in low and high mass values of  $m_{r,0} = 0.067$  kg and  $m_{r,0} = 0.6$  kg as well as low and high stiffness values of  $k_{r,0} = 0.1$  N/m and  $k_{r,0} = 0.9$  N/m. As mentioned before, case

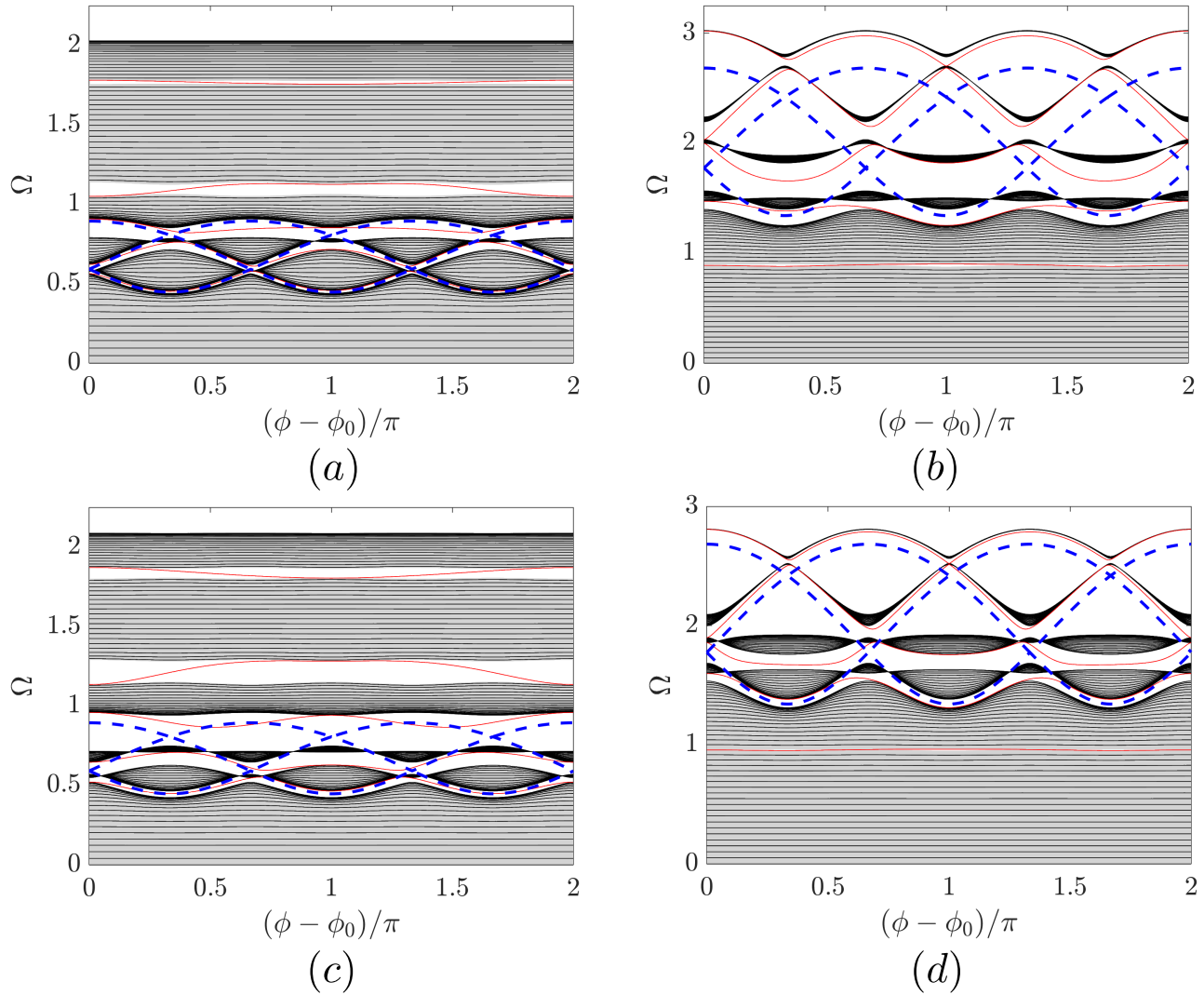


FIG. 9. Finite and Infinite band structures for case two with variations in either the average resonator stiffness,  $k_{r,0}$ , or average resonator mass,  $m_{r,0}$ . Resonator parameters are (a) standard average mass,  $m_{r,0} = 0.2$  kg and one third the standard average stiffness  $k_{r,0} = 0.1$  N/m (b) standard average mass,  $m_{r,0} = 0.2$  kg and triple the standard average stiffness  $k_{r,0} = 0.9$  N/m (c) standard average stiffness,  $k_{r,0} = 0.3$  N/m and triple the standard average mass  $m_{r,0} = 0.6$  kg and (d) standard average stiffness,  $k_{r,0} = 0.3$  N/m and one third the standard average mass  $m_{r,0} = 1/15$  kg.

three uses different stiffness values resulting in low and high values of  $k_{r,0} = 0.064$  N/m and  $k_{r,0} = 0.576$  N/m. As expected, the resonator frequency range can be shifted up or down by manipulating the resonator parameters. In Fig. 9(a),(c) and Fig. 10(a),(c), the resonator frequency range is moved to a lower frequency than in Fig. 4(b)-(c) by either decreasing the average resonator stiffness or increasing the average resonator mass. Likewise, in Fig. 9(b),(d) and Fig. 10(b),(d), the resonator frequency range is moved to a higher frequency by either increasing the average resonator stiffness or decreasing the average resonator mass. When shifting this range to lower frequencies, there is not a significant decrease in the upper limit of the uppermost passband. As such, with more bandgaps shifted to lower frequencies, there are fewer bandgaps in the upper frequency range, and the space is dominated by just one or two passbands. Rather than the bandgaps

growing to fill this spectral region, the passbands instead grow very wide causing the upper bandgaps to shrink significantly. For example, in Fig. 4(b), the two uppermost passbands cover a frequency range of 0.31 at  $\phi - \phi_0 = 0$  while in Fig. 9(a), the same passbands cover a much larger frequency range of 0.86. In some more extreme cases, like that found in Fig. 10(a), the upper bandgap may effectively disappear altogether leading to a merge in the upper two passbands. Furthermore, as these upper passbands shrink, they also oscillate less with the phase angle.

On the other hand, shifting the resonator frequency range upward (shown in Fig. 9(b),(d) and Fig. 10(b),(d)) produces an opposite result. As the resonator frequency range shifts upward, more bandgaps are brought into the higher frequency regime. This produces significantly wider passbands in the low frequency region with thin bandgaps disappearing in ex-

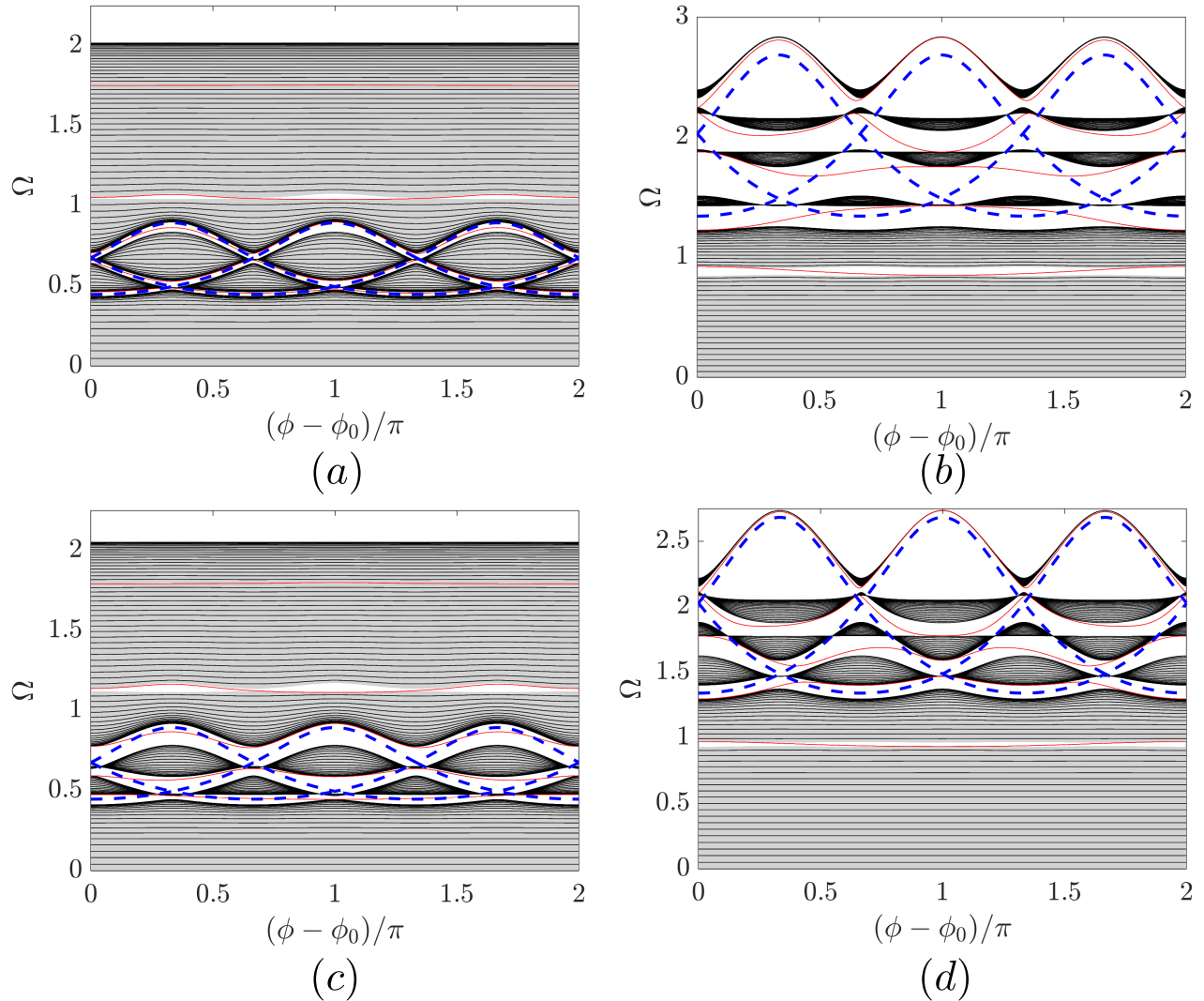


FIG. 10. Finite and Infinite band structures for case three with variations in either the average resonator stiffness,  $k_{r,0}$ , or average resonator mass,  $m_{r,0}$ . Resonator parameters are (a) standard average mass,  $m_{r,0} = 0.2$  kg and one third the standard average stiffness  $k_{r,0} = 0.064$  N/m (b) standard average mass,  $m_{r,0} = 0.2$  kg and triple the standard average stiffness  $k_{r,0} = 0.576$  N/m (c) standard average stiffness,  $k_{r,0} = 0.192$  N/m and triple the standard average mass  $m_{r,0} = 0.6$  kg and (d) standard average stiffness,  $k_{r,0} = 0.192$  N/m and one third the standard average mass  $m_{r,0} = 1/15$  kg.

tre cases such as in Fig. 9(d). Shifting the range upward does have a more significant impact on the upper limit of the uppermost passband though. As the resonator frequencies approach the upper limit of the band structure, the limit is pushed upward and begins to vary more dramatically to match the variation in the resonator frequencies. Despite the upper frequency limit of the band structure increasing, the upper passbands shrink drastically as the bandgaps become much wider. This results in multiple very thin passbands that oscillate significantly with changes in the phase angle. For example, in Fig. 10(d), the upper limit of the sixth passband oscillates between  $\Omega = 2.22$  and  $\Omega = 2.74$  while the upper limit of the same passband in Fig. 10(c) remains nearly constant at  $\Omega = 2.05$ .

While the band structure is strongly tied to the resonator frequency range, there are multiple methods to achieve the

same frequency range, and it is valuable to distinguish between additional effects of these methods. For example, the same resonator frequency range is achieved in Fig. 9(b),(d) and Fig. 10(b),(d), but the band structures are not the same. The range can be increased or decreased by changing either  $k_{r,0}$  or  $m_{r,0}$ , but the choice of parameters can determine other features such as bandgap size. A major trend to note is the effect that the resonator mass has on the bandgap sizes. When comparing band structures with the same resonator frequency range, like Fig. 10(a) and (c), for example, the system with a larger average resonator mass,  $m_{r,0}$ , will have larger bandgaps within its resonator frequency range. The parameter being modulated can also impact the band structure further. When modulation is found in the resonator mass,  $m_r$ , the bulk bands remain closer to the resonator frequencies at higher frequency ranges than when modulation is found in the resonator stiff-

This is the author's peer reviewed, accepted manuscript. However, the online version of record will be different from this version once it has been copyedited and typeset.  
PLEASE CITE THIS ARTICLE AS DOI: 10.1063/1.50203937

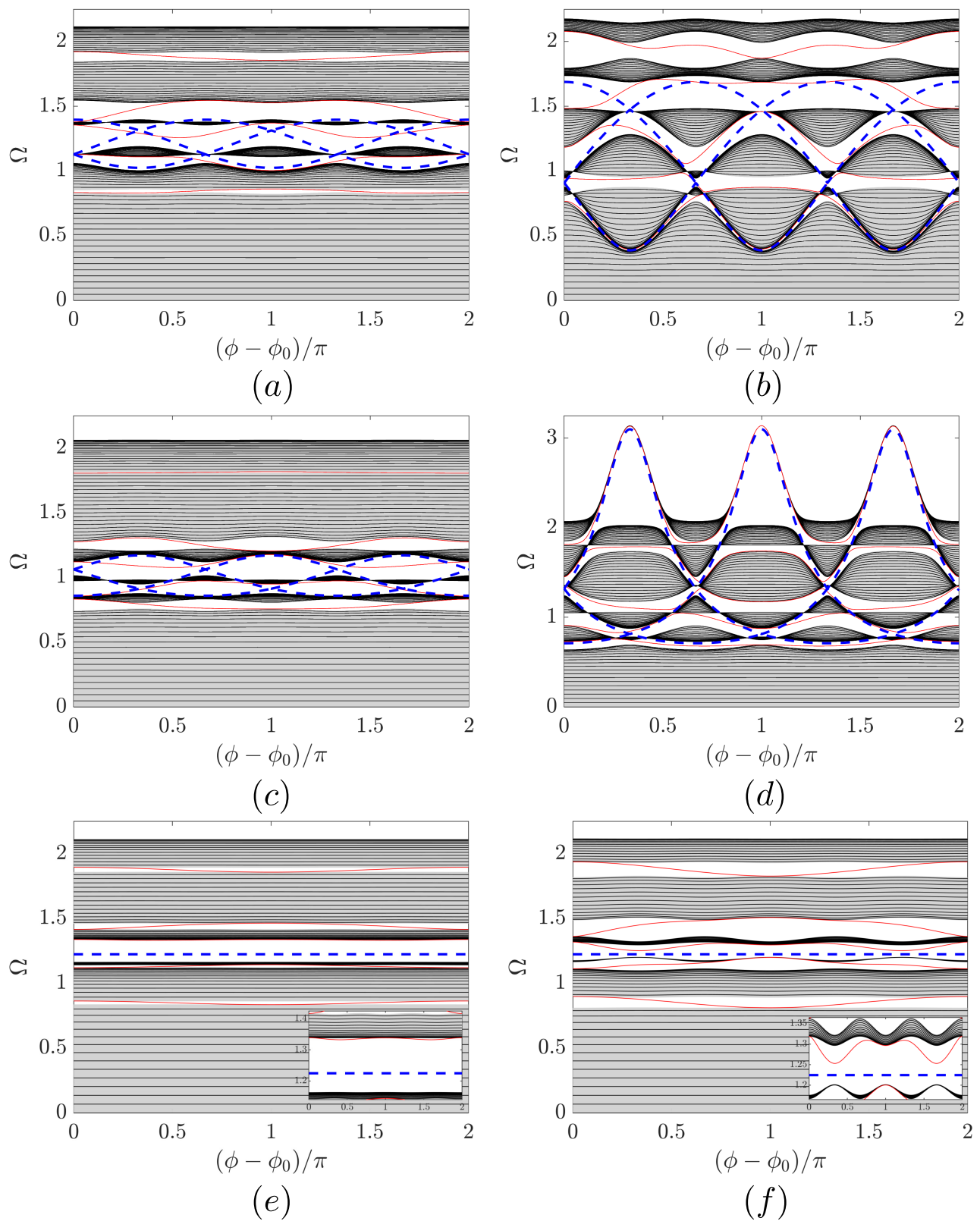


FIG. 11. Effect of changing modulation amplitude,  $\lambda$ , on the band structures of cases two (first row), three (second row), and four (third row) with low modulation amplitude,  $\lambda = 0.3$  (left columns), and high modulation amplitude,  $\lambda = 0.9$  (right columns). Standard resonator parameters of  $k_{r,0} = 0.3$  N/m and  $m_{r,0} = 0.2$  kg are used in cases two and four (a), (b), (e), (f), and standard resonator parameters of  $k_{r,0} = 0.192$  N/m and  $m_{r,0} = 0.2$  kg are used in case two (c), (d). The inset figures in (e)-(f) display zoomed in views of the third and fourth passbands.

This is the author's peer reviewed, accepted manuscript. However, the online version of record will be different from this version once it has been copyedited and typeset.  
PLEASE CITE THIS ARTICLE AS DOI: 10.1063/1.50203937

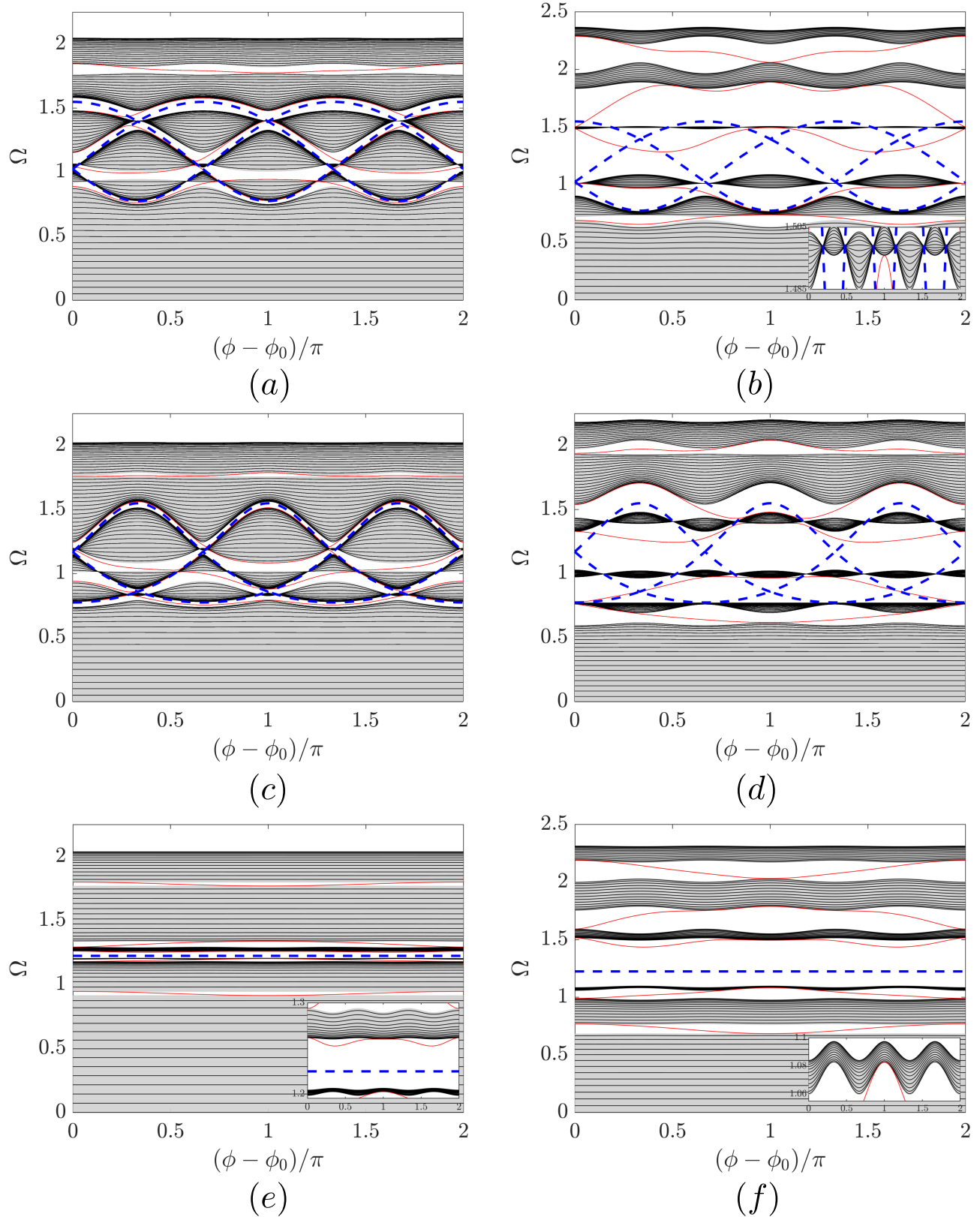


FIG. 12. Effect of changing both resonator stiffness and mass simultaneously on band structures with identical resonator frequency range for cases two (a)-(b), three (c)-(d), and four (e)-(f) with low parameters (left column figures), and high parameters (right column figures). Low parameters are one-third the standard resonator parameters, and high parameters are triple the standard values. This yields low resonator parameters of  $k_{r,0} = 0.1$  N/m and  $m_{r,0} = 1/15$  kg for cases two (a) and four (e) and  $k_{r,0} = 0.064$  N/m and  $m_{r,0} = 1/15$  kg for case three (c). High parameters are  $k_{r,0} = 0.9$  N/m and  $m_{r,0} = 0.6$  kg for cases two (b) and four (f) and  $k_{r,0} = 0.576$  N/m and  $m_{r,0} = 0.6$  kg for case three (d). Inset figures zoom in on the fourth bandgap in (b), third and fourth, bandgap in (e), and third bandgap in (f).

ness,  $k_r$ . This can be seen when comparing Fig. 9(b) and Fig. 10(b). Both cases share the same resonator frequency range, and both experience an increase in the upper limit of their uppermost passband. However, in the case with modulation in the resonator stiffness (Fig. 9(b)), the upper band is pushed much further upward by the maximum resonator frequency. On the other hand, when modulation is in the resonator mass (Fig. 10(b)), the upper band clings tightly to the maximum resonator frequency and does not shift to as high of a frequency as in the previous case. This is seen most clearly in Fig. 10(d) where the uppermost passband is nearly identical to the maximum resonator frequency.

While changing a single parameter can shift the resonator frequency range to higher or lower frequencies, it also changes the size of the frequency range. By increasing (decreasing) the average resonator frequency, the resonator frequency range also increases (decreases) in size. It is not possible to shift the resonator frequency range without also changing its size. However, it is possible instead to change the size of the resonator frequency range without changing its location. As long as the average resonator frequency,  $\omega_{r,0}$ , remains constant, the range will not change in location. This can be achieved by changing the amplitude of modulation,  $\lambda$ . Figure 11 shows the band structures for cases 2-4 with higher and lower modulation amplitudes. The plots in the left column show that for lower modulation amplitude, the size of the resonator frequency range is greatly reduced. Similarly, for higher modulation amplitude, the range is increased. By changing the amplitude of modulation, the resonator frequency range changes size, but its location, defined by the average resonator frequency,  $\omega_{r,0}$ , remains constant. As the modulation amplitude increases, the passbands and bandgaps experience significantly greater variation with the phase angle. Despite the bandgap sizes changing more dramatically with the phase, the total combined width of the bandgaps also increases as the modulation amplitude increases. This trend can even be found in case four in Fig. 11(e)-(f) with a single constant resonator frequency. Even though the resonator frequency remains constant, the increase in variation of the resonator parameters leads to an increase in bandgap size and variation.

While increasing the bandgap size in this way can be beneficial, the increase in variation can actually be more detrimental to the system dynamics. As mentioned before, we can sometime see the existence of multiple passbands that overlap in frequency range at different phase variables. In these instances, there is no complete bandgap across all phase angles. When the variation in bandgap and passbands increases, these instances occur more commonly and display larger areas of overlap. This can be seen most strongly in Fig. 11(b). When compared to the standard case with lower  $\lambda$  in Fig. 4(b), the overlap originally found in the first bandgap increases significantly to account for almost the entire second passband, and the third bandgap goes from having no overlap to having substantial overlap from its adjacent passbands. It is possible to remediate the overlap of passbands by increasing the bandgap width through careful selection of the average resonator parameters which is detailed below. However, at higher modulation amplitudes, this becomes a much greater challenge.

Although the resonator frequency range is strongly influential to the band structure, it is not the only determining factor in bandgap formation. Even without changing the resonator frequency range, the individual resonator parameters can significantly alter the band structure. Figure 12 shows the band structures for cases 2-4 with the same resonator frequency range but different resonator parameters. Since the resonator frequency range is directly tied to the average resonator frequency, changes made to both the resonator mass and stiffness that do not change the ratio between them,  $k_{r,0}/m_{r,0}$ , will have no impact on the resonator frequency range. As seen in Fig. 12, increasing both the mass and the stiffness will increase the bandgap size in all three cases without changing the resonator frequency range. This observation demonstrates strong alignment with findings previously documented in the literature regarding the impact of the local resonator's mass on the bandgap's size<sup>61</sup>. More specifically, the change in bandgap size effects the middle bandgap most strongly with effects diminishing as you move to further bandgaps above or below it. If the resonator parameters are lowered enough, we can observe, as before, significantly overlapping passbands due to the bandgaps still oscillating with the phase despite being very thin. But through increasing the parameters, this overlap disappears. These trends also hold true for case four in Fig. 12(e)-(f) showing larger bandgaps with larger resonator parameters even with a single resonator frequency.

### C. Mode Shapes

The pronounced effect that comes from modulating the resonator parameters appears not only in changes to the band structure, but also in the mode shapes. From the band structure, we observed the presence of an additional mode spanning the middle bandgap as well as changes to the other edge modes. These changes are reflected here in the mode shapes. When a finite chain is excited at a frequency within a topological bandgap, edge localized vibration modes arise. These edge modes have been well documented in previous studies, so an in depth discussion of most of the edge modes will be withheld. Instead, greater attention will be given to two major differences in the mode shapes that are caused by modulating the resonator parameters rather than the main chain parameters.

The first major difference is the existence of an additional edge mode in the topologically trivial (third) bandgap which does not appear in the case with periodic resonators. To validate the existence of this edge mode, the mode shapes of main mass displacement are plotted in Fig. 13 for cases 2-4 when excited within the third bandgap. Case one is excluded here because in this case, there is no additional mode present within the third bandgap. As such, there is no vibration mode to display. Here, the system consists of a finite chain with 60 cells, and the mode shapes are shown to vary over a full range of the phase variable. For better visualization, the mode shapes are normalized to the maximum value of mass displacement within that mode. With each case, vibrations are localized to one edge of the chain or the other. Even though

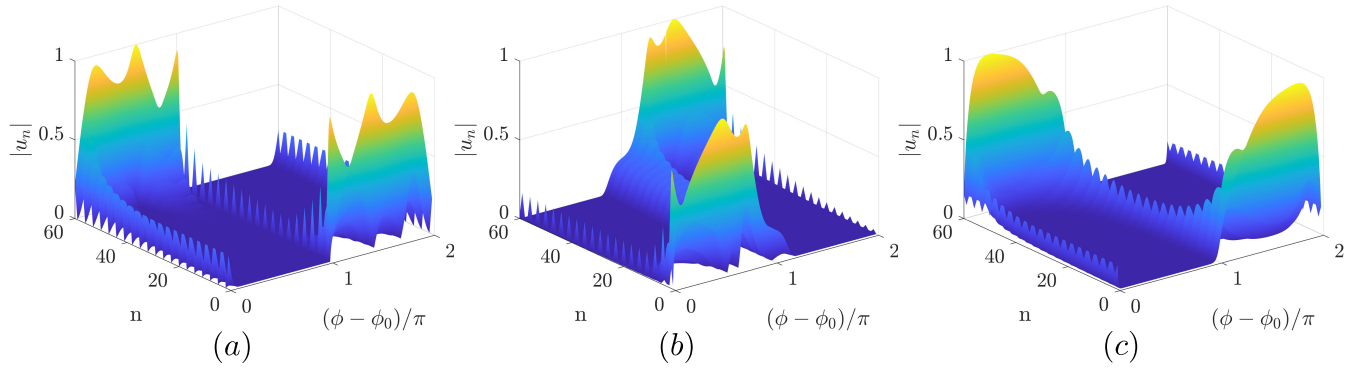


FIG. 13. Displacement mode shapes varying with phase angle,  $\phi$ , for cases 2-4 (a)-(c), respectively, with standard parameters and excited along the additional mode within the third bandgap.

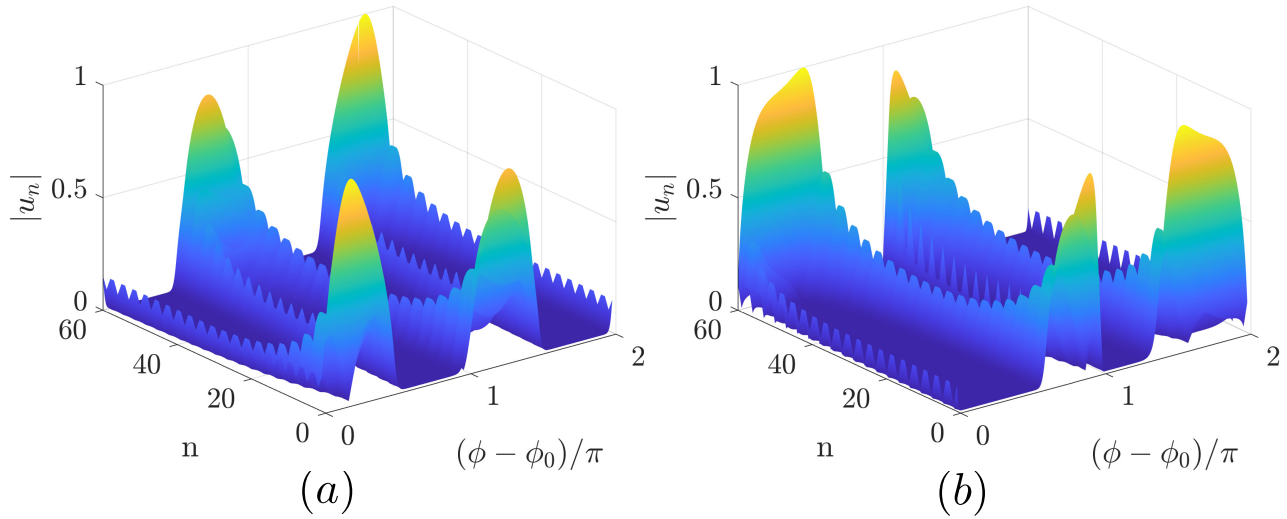


FIG. 14. Displacement mode shapes varying with phase angle for case two in the fourth bandgap (a) and case three in the second bandgap showing two topological pumping cycles in a full phase cycle.

the additional edge mode does not span the entire width of the bandgap, the mode follows the same behavior of other edge modes. At one end of the phase spectrum, with  $\phi - \phi_0 = 0$ , the edge mode frequencies are joined to a bulk passband as shown in Fig. 4, and the localization is focused on one end of the chain. As the phase increases, the edge mode frequency separates from the passband, increasing the degree of localization before momentarily returning to the passband again at  $\phi - \phi_0 = \pi$ . The effect of this on the mode shapes is evident in Fig. 13. In each case, the vibration is localized to one end of the chain, and at the point  $\phi - \phi_0 = \pi$ , as the mode frequency touches the passband, the location of vibration localization switches to the opposite end.

The other major difference is found in how the edge modes approach and touch their adjacent bulk bands. When modulation is found in the main chain stiffness, the frequency of an edge mode will span its bandgap a number of times corresponding to the magnitude of the bandgap's Chern number,  $|C_g|$ . For example, in a bandgap with  $|C_g| = 1$ , the edge mode frequency will approach one passband, touch it once, then turn to approach the other passband and touch it once all within a

full  $2\pi$  phase cycle. This results in the edge mode migrating from one edge to the other when the frequency touches a passband. This is also the case when both the resonator mass and stiffness are modulated together, as in case four. However, there are exceptions to this trend when a single resonator parameter is modulated. For some bandgaps with  $|C_g| = 1$ , rather than only touching each passband once, the edge mode frequency will sometimes touch one passband, remain close to it, and touch the same passband two more times before crossing the bandgap to touch the other passband. This can be seen in Fig. 4(b)-(c) for case two within the fourth bandgap and case three within the second bandgap, respectively. The mode shapes are given in Fig. 14 for the two bandgaps mentioned above. For instances such as these, the edge mode frequency comes into contact with the adjacent passbands not twice, but four times. Each time it does so, the vibration localization switches from one edge to the other. This can be validated in Fig. 14(a) by noting that it switches localization at phase angles of  $\phi - \phi_0 = 0.5\pi, 1\pi$ , and  $1.5\pi$ . These correspond directly to the points in Fig. 4(b) where the edge mode frequency touches the passband. Because  $|C_g| = 1$  for these bandgaps,

the edge mode frequency only fully spans its bandgap once, but despite this, the mode migration resembles the migration of mode shapes with Chern numbers greater than one, such as those reported by Liao and Zhou<sup>54</sup>. For purposes where the phase angle is actively being cycled, such as for topological pumping, this faster migration of edge modes can be quite valuable. In traditional cases, the phase angle would need to be modulated by an entire half cycle from  $0 - \pi$  to pump a localized wave from one end of the chain to the other. Within these bandgaps however, localization switches direction more times within one cycle. This allows for pumping of the wave from one edge to the other in half of the previous phase cycle. For systems with time varying phase, this can lead to faster transportation of mechanical energy along the chain.

#### IV. CONCLUSIONS

In this paper, we investigated the mechanisms behind bandgap formation in metamaterials due to combined effects from local resonance and spatial modulation of resonator parameters. The metamaterial studied was modeled as a 1-dimensional lattice of masses connected by springs with each mass coupled to a local resonator modeled as a spring-mass system. Spatial modulation of parameters was present for different cases consisting of modulation in the main chain stiffness, resonator stiffness, resonator mass, or combinations of those sources. The dispersion relations for infinite chains were obtained analytically through analysis of the unit cell. These results were validated numerically for finite chains using eigenvalue analysis. The mode shapes were also determined for finite chains from the eigenvectors. Both the formation mechanism and topological nature of each bandgap were revealed. Furthermore, the band structures were plotted for a variety of sources of modulation as well as for a variety of resonator parameters to determine how the patterning and local resonance interact to form bandgaps.

The results indicate that moving parameter modulation from the main chain stiffness to the resonator parameters significantly alters the band structure. With the presence of modulated resonators, multiple locally resonant bandgaps form from bandgaps previously opened by Bragg scattering. By changing these bandgaps to locally resonant bandgaps, the vibration attenuation performance was improved. The topologically trivial bandgap hosted an additional edge mode while remaining topologically trivial. The phase of the edge states was also shifted asymmetrically. Due to having multiple unique resonators, the local resonance phenomena was not defined by a single resonator frequency, but by a resonator frequency range which holds significant influence over the band structure. Within this range, there occurs multiple points in the band structure at which some passbands disappear and the adjacent bandgaps merge. As the passband closes and reopens, the adjacent bandgaps also undergo transitions between locally resonant and Bragg scattering bandgaps. These points reveal a new method for determining the number and type of bandgaps in a system that is independent of the modulation parameter. It has also been demonstrated that both the size and

location of the resonator frequency range can be tuned through judicious choice of the resonator parameters and modulation amplitude. By changing one parameter to increase the average resonator frequency, the range can be shifted upward and grow. Changing the modulation amplitude can also change the size of the range without altering its location. From the mode shapes, we validated that the additional edge mode present in the middle bandgap hosts localized vibrations. Furthermore, we observed the presence of edge states with faster pumping of the vibration localization from edge to edge. Rather than taking a full  $2\pi$  to pump the wave from one edge to the next and back, these edge states can pump the wave back and forth in half the phase.

In conclusion, for metamaterials with spatially modulated resonators, the band structure is strongly determined by both the resonator parameters and the location and strength of modulation. Methods of tuning these complex band structures have been outlined through careful selection of resonator parameters. A study of the mode shapes revealed the presence of an additional edge mode as well as vibration localization that switches direction with greater frequency. Because of their dependence on resonator parameters and patterning, these phenomena have the potential to be introduced to many non-resonant materials with any kind of structure. This paves the way for strongly adaptable metamaterials with features valuable for a variety of applications including wave guiding, energy harvesting, topological pumping, and wave nonreciprocity.

#### ACKNOWLEDGMENTS

This work is supported in part by the National Science Foundation (NSF) Grant CMMI-2038187.

#### AUTHOR DECLARATIONS

##### Conflict of Interest Statement

The authors have no conflicts to disclose.

#### Author Contributions

**Joshua LeGrande:** Formal analysis (lead); investigation (lead); methodology (equal); writing - original draft (lead); writing - review and editing (equal). **Arun Malla:** Methodology (equal); writing - review and editing (equal). **Mohammad Bukhari:** Conceptualization (equal); funding acquisition (equal); supervision (equal); writing - review and editing (equal). **Oumar Barry:** Conceptualization (equal); funding acquisition (equal); project administration (lead); supervision (equal); writing - review and editing (equal).

## DATA AVAILABILITY STATEMENT

The data that support the findings of this study are available from the corresponding author upon reasonable request.

- <sup>1</sup>M. I. Hussein, M. J. Leamy, and M. Ruzzene, “Dynamics of phononic materials and structures: Historical origins, recent progress, and future outlook,” *Applied Mechanics Reviews* **66**, 040802 (2014).
- <sup>2</sup>K. Bertoldi, V. Vitelli, J. Christensen, and M. van Hecke, “Flexible mechanical metamaterials,” *Nature Reviews Materials* **2**, 17066 (2017).
- <sup>3</sup>W. Cai and V. M. Shalaev, *Optical Metamaterials*, Vol. 10 (Springer, 2010).
- <sup>4</sup>R. Martínez-Sala, J. Sancho, J. V. Sánchez, V. Gómez, J. Llinares, and F. Meseguer, “Sound attenuation by sculpture,” *Nature* **378**, 241–241 (1995).
- <sup>5</sup>J. Christensen, M. Kadic, O. Kraft, and M. Wegener, “Vibrant times for mechanical metamaterials,” *MRS Communications* **5**, 453–462 (2015).
- <sup>6</sup>R. Zhu, X. Liu, G. Hu, C. Sun, and G. Huang, “A chiral elastic metamaterial beam for broadband vibration suppression,” *Journal of Sound and Vibration* **333**, 2759–2773 (2014).
- <sup>7</sup>Y. Li, E. Baker, T. Reissman, C. Sun, and W. K. Liu, “Design of mechanical metamaterials for simultaneous vibration isolation and energy harvesting,” *Applied Physics Letters* **111**, 251903 (2017).
- <sup>8</sup>F. Zangeneh-Nejad, D. L. Sounas, A. Alù, and R. Fleury, “Analogue computing with metamaterials,” *Nature Reviews Materials* **6**, 207–225 (2021).
- <sup>9</sup>Z. Lu, Z. Wang, Y. Zhou, and X. Lu, “Nonlinear dissipative devices in structural vibration control: A review,” *Journal of Sound and Vibration* **423**, 18–49 (2018).
- <sup>10</sup>A. Darabi, A. Zareei, M.-R. Alam, and M. J. Leamy, “Experimental demonstration of an ultrabroadband nonlinear cloak for flexural waves,” *Physical Review Letters* **121**, 174301 (2018).
- <sup>11</sup>M. I. Rosa, R. K. Pal, J. R. Arruda, and M. Ruzzene, “Edge states and topological pumping in spatially modulated elastic lattices,” *Physical Review Letters* **123**, 034301 (2019).
- <sup>12</sup>Y. Achaoui, V. Laude, S. Benchabane, and A. Khelif, “Local resonances in phononic crystals and in random arrangements of pillars on a surface,” *Journal of Applied Physics* **114**, 104503 (2013).
- <sup>13</sup>M. M. Sigalas and E. N. Economou, “Elastic and acoustic wave band structure,” *Journal of Sound and Vibration* **158**, 377–382 (1992).
- <sup>14</sup>M. Sigalas and E. N. Economou, “Band structure of elastic waves in two dimensional systems,” *Solid State Communications* **86**, 141–143 (1993).
- <sup>15</sup>M. S. Kushwaha, P. Halevi, L. Dobrzynski, and B. Djafari-Rouhani, “Acoustic band structure of periodic elastic composites,” *Physical Review Letters* **71**, 2022 (1993).
- <sup>16</sup>M. S. Kushwaha, P. Halevi, G. Martinez, L. Dobrzynski, and B. Djafari-Rouhani, “Theory of acoustic band structure of periodic elastic composites,” *Physical Review B* **49**, 2313 (1994).
- <sup>17</sup>J. Vasseur, B. Djafari-Rouhani, L. Dobrzynski, M. Kushwaha, and P. Halevi, “Complete acoustic band gaps in periodic fibre reinforced composite materials: the carbon/epoxy composite and some metallic systems,” *Journal of Physics: Condensed Matter* **6**, 8759 (1994).
- <sup>18</sup>M. S. Kushwaha, “Classical band structure of periodic elastic composites,” *International Journal of Modern Physics B* **10**, 977–1094 (1996).
- <sup>19</sup>Z. Liu, X. Zhang, Y. Mao, Y. Zhu, Z. Yang, C. T. Chan, and P. Sheng, “Locally resonant sonic materials,” *Science* **289**, 1734–1736 (2000).
- <sup>20</sup>L. Liu and M. I. Hussein, “Wave motion in periodic flexural beams and characterization of the transition between bragg scattering and local resonance,” *Journal of Applied Mechanics* **79**, 011003 (2012).
- <sup>21</sup>G. Huang and C. Sun, “Band gaps in a multiresonator acoustic metamaterial,” *Journal of Vibration and Acoustics* **132**, 031003 (2010).
- <sup>22</sup>Y. Gao and L. Wang, “Ultrawide coupled bandgap in hybrid periodic system with multiple resonators,” *Journal of Applied Physics* **127** (2020).
- <sup>23</sup>Y. Xia, M. Ruzzene, and A. Erturk, “Dramatic bandwidth enhancement in nonlinear metastructures via bistable attachments,” *Applied Physics Letters* **114**, 093501 (2019).
- <sup>24</sup>G. Hu, L. Tang, and R. Das, “Internally coupled metamaterial beam for simultaneous vibration suppression and low frequency energy harvesting,” *Journal of Applied Physics* **123**, 055107 (2018).
- <sup>25</sup>H. Meng, D. Chronopoulos, A. Fabro, W. Elmadih, and I. Maskery, “Rainbow metamaterials for broadband multi-frequency vibration attenuation: Numerical analysis and experimental validation,” *Journal of Sound and Vibration* **465**, 115005 (2020).
- <sup>26</sup>M. Alshaqqaq and A. Erturk, “Graded multifunctional piezoelectric metastructures for wideband vibration attenuation and energy harvesting,” *Smart Materials and Structures* **30**, 015029 (2020).
- <sup>27</sup>K. Yi and M. Collet, “Broadening low-frequency bandgaps in locally resonant piezoelectric metamaterials by negative capacitance,” *Journal of Sound and Vibration* **493**, 115837 (2021).
- <sup>28</sup>F. Casadei, T. Delpero, A. Bergamini, P. Ermanni, and M. Ruzzene, “Piezoelectric resonator arrays for tunable acoustic waveguides and metamaterials,” *Journal of Applied Physics* **112**, 064902 (2012).
- <sup>29</sup>O. Thorp, M. Ruzzene, and A. Baz, “Attenuation and localization of wave propagation in rods with periodic shunted piezoelectric patches,” *Smart Materials and Structures* **10**, 979 (2001).
- <sup>30</sup>A. Bergamini, T. Delpero, L. D. Simoni, L. D. Lillo, M. Ruzzene, and P. Ermanni, “Phononic crystal with adaptive connectivity,” *Advanced Materials* **26**, 1343–1347 (2014).
- <sup>31</sup>M. Bukhari and O. Barry, “Spectro-spatial analyses of a nonlinear metamaterial with multiple nonlinear local resonators,” *Nonlinear Dynamics* **99**, 1539–1560 (2020).
- <sup>32</sup>L. Yu, L. Tang, L. Xiong, T. Yang, and B. R. Mace, “A passive self-tuning nonlinear resonator with beam-slider structure,” in *Active and Passive Smart Structures and Integrated Systems XII*, Vol. 10967 (International Society for Optics and Photonics, 2019) p. 109670K.
- <sup>33</sup>M. A. Bukhari and O. R. Barry, “Towards a self tuning sliding mass metastructure,” *Scientific reports* **11**, 21630 (2021).
- <sup>34</sup>G. Ma, M. Xiao, and C. T. Chan, “Topological phases in acoustic and mechanical systems,” *Nature Reviews Physics* **1**, 281–294 (2019).
- <sup>35</sup>S. H. Mousavi, A. B. Khanikaev, and Z. Wang, “Topologically protected elastic waves in phononic metamaterials,” *Nature Communications* **6**, 1–7 (2015).
- <sup>36</sup>M. Miniaci, R. Pal, B. Morvan, and M. Ruzzene, “Experimental observation of topologically protected helical edge modes in patterned elastic plates,” *Physical Review X* **8**, 031074 (2018).
- <sup>37</sup>R. Chaunsali, C.-W. Chen, and J. Yang, “Subwavelength and directional control of flexural waves in zone-folding induced topological plates,” *Physical Review B* **97**, 054307 (2018).
- <sup>38</sup>S. Aubry and G. André, “Analyticity breaking and anderson localization in incommensurate lattices,” *Ann. Israel Phys. Soc* **3**, 18 (1980).
- <sup>39</sup>D. J. Apigo, K. Qian, C. Prodan, and E. Prodan, “Topological edge modes by smart patterning,” *Physical Review Materials* **2**, 124203 (2018).
- <sup>40</sup>X. Ni, K. Chen, M. Weiner, D. J. Apigo, C. Prodan, A. Alù, E. Prodan, and A. B. Khanikaev, “Observation of hofstadter butterfly and topological edge states in reconfigurable quasi-periodic acoustic crystals,” *Communications Physics* **2**, 1–7 (2019).
- <sup>41</sup>R. K. Pal, M. I. Rosa, and M. Ruzzene, “Topological bands and localized vibration modes in quasiperiodic beams,” *New Journal of Physics* **21**, 093017 (2019).
- <sup>42</sup>X. Pu, A. Palermo, and A. Marzani, “Topological edge states of quasiperiodic elastic metasurfaces,” *Mechanical Systems and Signal Processing* **181**, 109478 (2022).
- <sup>43</sup>Y. Xia, A. Erturk, and M. Ruzzene, “Topological edge states in quasiperiodic locally resonant metastructures,” *Physical Review Applied* **13**, 014023 (2020).
- <sup>44</sup>M. I. Rosa, M. J. Leamy, and M. Ruzzene, “Amplitude-dependent edge states and discrete breathers in nonlinear modulated phononic lattices,” *New Journal of Physics* **25**, 103053 (2023).
- <sup>45</sup>J. LeGrande, M. Bukhari, and O. Barry, “Topological properties and localized vibration modes in quasiperiodic metamaterials with electromechanical local resonators,” in *International Design Engineering Technical Conferences and Computers and Information in Engineering Conference*, Vol. 86311 (American Society of Mechanical Engineers, 2022) p. V010T10A004.
- <sup>46</sup>D. R. Hofstadter, “Energy levels and wave functions of bloch electrons in rational and irrational magnetic fields,” *Physical Review B* **14**, 2239 (1976).
- <sup>47</sup>E. Riva, V. Casieri, F. Resta, and F. Braghin, “Adiabatic pumping via avoided crossings in stiffness-modulated quasiperiodic beams,” *Physical Review B* **102**, 014305 (2020).
- <sup>48</sup>E. Riva, M. I. Rosa, and M. Ruzzene, “Edge states and topological pumping in stiffness-modulated elastic plates,” *Physical Review B* **101**, 094307 (2020).

This is the author's peer reviewed, accepted manuscript. However, the online version of record will be different from this version once it has been copyedited and typeset.

PLEASE CITE THIS ARTICLE AS DOI: 10.1063/5.0203937

- (2020).
- <sup>49</sup>Y. Xia, E. Riva, M. I. Rosa, G. Cazzulani, A. Erturk, F. Braghin, and M. Ruzzene, "Experimental observation of temporal pumping in electromechanical waveguides," *Physical Review Letters* **126**, 095501 (2021).
- <sup>50</sup>J. LeGrande, M. Bukhari, and O. Barry, "Effect of electromechanical coupling on locally resonant quasiperiodic metamaterials," *AIP Advances* **13**, 015112 (2023).
- <sup>51</sup>M. I. Rosa, Y. Guo, and M. Ruzzene, "Exploring topology of 1d quasiperiodic metastructures through modulated lego resonators," *Applied Physics Letters* **118**, 131901 (2021).
- <sup>52</sup>Y. Chen, X. Li, H. Nassar, A. N. Norris, C. Daraio, and G. Huang, "Nonreciprocal wave propagation in a continuum-based metamaterial with space-time modulated resonators," *Physical Review Applied* **11**, 064052 (2019).
- <sup>53</sup>M. Attarzadeh, J. Callanan, and M. Nouh, "Experimental observation of nonreciprocal waves in a resonant metamaterial beam," *Physical Review Applied* **13**, 021001 (2020).
- <sup>54</sup>Y. Liao and X. Zhou, "Topological pumping in doubly modulated mechanical systems," *Physical Review Applied* **17**, 034076 (2022).
- <sup>55</sup>J. Marconi, E. Riva, M. Di Ronco, G. Cazzulani, F. Braghin, and M. Ruzzene, "Experimental observation of nonreciprocal band gaps in a space-time-modulated beam using a shunted piezoelectric array," *Physical Review Applied* **13**, 031001 (2020).
- <sup>56</sup>H. Nassar, H. Chen, A. Norris, M. Haberman, and G. Huang, "Nonreciprocal wave propagation in modulated elastic metamaterials," in *Proceedings of the Royal Society A: Mathematical, Physical, and Engineering Sciences*, Vol. 473 (2017).
- <sup>57</sup>H. Nassar, X. Xu, A. Norris, and G. Huang, "Modulated phononic crystals: Non-reciprocal wave propagation and willis materials," *Journal of the Mechanics and Physics of Solids* **101**, 10–29 (2017).
- <sup>58</sup>Y. Hatsugai, "Chern number and edge states in the integer quantum hall effect," *Physical review letters* **71**, 3697 (1993).
- <sup>59</sup>T. Fukui, Y. Hatsugai, and H. Suzuki, "Chern numbers in discretized brillouin zone: efficient method of computing (spin) hall conductances," *Journal of the Physical Society of Japan* **74**, 1674–1677 (2005).
- <sup>60</sup>M. I. Rosa, B. L. Davis, L. Liu, M. Ruzzene, and M. I. Hussein, "Material vs. structure: Topological origins of band-gap truncation resonances in periodic structures," *Physical Review Materials* **7**, 124201 (2023).
- <sup>61</sup>D. J. Inman, *Engineering vibration*, Vol. 3.